Inorg. Chem. **2009**, *48*, 3323−3341

Inorganic Chemistry
Article

Forum

Magnetic [$n \times n$] ($n = 2-5$) Grids by Directed Self-Assembly

Louise N. Dawe, Konstantin V. Shuvaev, and Laurence K. Thompson*

Department of Chemistry, Memorial University, St. John's, Newfoundland A1B 3X7, Canada

Received June 12, 2008

Polytopic hydrazone-based ligands are discussed in the context of the design attributes of the ligand and the power of self-assembly as a methodology for the synthesis of polymetallic systems with specific and predetermined organization of the metal centers in a closely spaced bridged arrangement. Magnetic exchange coupling occurs as a result of the close proximity of the metal ions. Homometallic, heterometallic, and mixed-spin-state [$n \times n$] ($n = 2-5$) square grids are highlighted and discussed in terms of their structural and magnetic properties. Antiferromagnetic, ferromagnetic, and ferrimagnetic examples are described.

Introduction

The quest for novel materials has brought a distinct focus on the chemistry community, and in the area of metal-based compounds, electronic, photophysical, photochemical, catalytic, and magnetic properties have seen intense interest. With metal-based systems, polynuclear complexes have received, and continue to receive, significant attention. The synthetic challenge involves finding simple, efficient, and yet logical approaches to the incorporation of large numbers of metal ions in a small, single molecular entity and also to build into the resulting system useful molecular-based properties. Single-molecule magnets (SMMs) have risen to the forefront in this area as potential systems for nanoscale devices with possible future applications in microelectronic and high-resolution magnetic technologies. Many examples of high-nuclearity, SMM systems have been produced ranging from simple dinuclear to very high-nuclearity complexes, most of which are based on manganese as the paramagnetic metal ion and have Mn^{III} or Mn^{IV} sites as essential components, with Jahn−Teller axis distortions as a major element resulting in single-ion anisotropy and SMM behavior.[1−4] Critical temperatures for most systems studied have so far been very low (<5 K), clearly indicating that thermal energy barriers to magnetization loss are much too low for practical use. Enhancing such properties is a challenge.

Polynuclear aggregates have been approached by two main methods: (1) using relatively simple ligands with ambident or ampolydentate character, with appended potentially bridging groups, e.g., R−O$^-$ and carboxylate, which serve to aggregate metal ions in a polynuclear cluster through a network of bridges, or (2) using large polytopic ligands with "designed" arrays of coordination pockets suitably juxtaposed to create specific geometric arrangements of metal ions through bridging connections, e.g., R−O$^-$ and R−N−N−R′, built into the ligand backbone. The most studied of this group comprise homoleptic [$n \times n$] grids. The former approach has led to spectacular examples of very high-nuclearity clusters but in large measure through serendipitous assembly using simple ligands like carboxylates and exogenous bridges, e.g., oxide, hydroxide, alkoxide,[1−4] and polyfunctional ligands, e.g., pyridonates,[5] tripodal alcohols,[6] tripodal carboxylic acids,[7] salicylaldoximes,[8] and dipyridyl ketones.[9,10] The latter approach, which forms the general theme

* To whom correspondence should be addressed. E-mail: lthomp@mun.ca. Tel: 709-737-8750. Fax: 709-737-3702.

(1) Sessoli, R.; Gatteschi, D.; Caneschi, A.; Novak, M. A. *Nature* **1993**, *365*, 141–143.
(2) Sessoli, R.; Gatteschi, D. *Angew. Chem., Int. Ed.* **2003**, *42*, 268–297.
(3) Christou, G. *Polyhedron* **2005**, *24*, 2065–2075, and references cited therein.
(4) Gatteschi, D.; Sessoli, R.; Villain, J. *Molecular Nanomagnets*; Oxford University Press: Oxford, U.K., 2006.
(5) Winpenny, R. E. P. *J. Chem. Soc., Dalton Trans.* **2002**, 1–10.
(6) Brechin, E. K. *Chem. Commun.* **2005**, 5141–5153.
(7) Murugesu, M.; Clérac, R.; Anson, C. E.; Powell, A. K. *Inorg. Chem.* **2004**, *43*, 7269–7271.
(8) Milios, C. J.; Piligkos, S.; Brechin, E. K. *Dalton Trans.* **2008**, 1809–1817.
(9) Tangoulis, V.; Raptopoulou, C. P.; Terzis, A.; Paschalidou, S.; Perlepes, S. P.; Bakalbassis, E. G. *Inorg. Chem.* **1997**, *36*, 3996–4006.

10.1021/ic801078h CCC: $40.75
Published on Web 04/13/2009

of this paper, involves directed self-assembly where the polydentate nature of the ligand programs the metal−ligand interaction to produce [$n \times n$] grids with predetermined dimensions, with examples so far in the range M_4 to M_{25} ($n = 2-5$).[11−18] The close-bridged proximity of the metal ions in both classes of complex leads to magnetic exchange interactions, with antiferromagnetic, ferromagnetic, and ferrimagnetic examples and in some cases SMM behavior. This Forum Article will focus on both symmetric and asymmetric grids (based on polytopic ligand design) and homometallic and heterometallic grid complexes.

Experimental Section

Physical Measurements. IR spectra were recorded as Nujol mulls using a Mattson Polaris FT-IR instrument, and UV/vis spectra were obtained using a Cary 5E spectrometer. Microanalyses were carried out by Canadian Microanalytical Service, Delta, Canada. Variable-temperature magnetic data (2−300 K) were obtained using a Quantum Design MPMS5S SQUID magnetometer using field strengths in the range 0.1−5 T. Background corrections for the sample-holder assembly and diamagnetic components of the complexes were applied. NMR measurements were taken with a Bruker AVANCE 500 MHz spectrometer. Liquid chromatography/mass spectrometry (LC/MS) measurements were taken using an Agilent 1100 series LC/MSD in APCI mode with methanol and acetonitrile as the solvents.

X-ray data collection was carried out at 153(1) K on a Rigaku Saturn CCD area detector with graphite-monochromated Mo Kα radiation. Data were collected and processed using CrystalClear (Rigaku) and the CIF files are included as Supporting Information. Data were collected to at least 55° in 2θ, except for **18**, which was collected only to $2\theta = 46.4°$. The full cationic framework, however, was revealed for **18**, and so the CIF file for this compound has also been included in the Supporting Information.

Synthesis of Ligands. L1Me. 3,6-Dicarbomethoxypyridazine[19] (1.68 g, 8.57 mmol) was dissolved in MeOH (250 mL) upon heating at 50 °C. Hydrazine hydrate (0.40 g, 8.0 mmol) was added slowly in three portions as a solution in MeOH (15 mL) over the course of ∼12 h, and the mixture was allowed to stand for a further 12 h. The resulting pale-yellow powder was filtered off and dried (yield: 1.13 g, 67%). Characteristic IR bands showed conversion to the monohydrazone, 6-carbomethoxy-3-pyridazinecarboxylic acid hydrazide. Pyrazinecarbonitrile (0.24 g, 2.3 mmol) was dissolved in 15 mL of dry MeOH and a small amount of sodium added to catalyze the formation of the imidate ester. After heating at 40 °C for 50 min, the solution was neutralized with glacial acetic acid and 6-carbomethoxy-3-pyridazinecarboxylic acid hydrazide (0.40 g, 2.04 mmol) added as a suspension in 40 mL of dry MeOH. The mixture was refluxed for 1 day, after which a yellow precipitate was collected by filtration and dried in air. Yield: 0.51 g, 81%. Mp: 279−281 °C (dec). IR (ν/cm^{-1}, Nujol): 1599s ($\nu_{C=N}$), 1624s, 1681m, 1720s ($\nu_{C=O}$). LC/MS: 302 $[M + H]^+$.

Anal. Calcd (%) for $C_{12}H_{11}N_7O_3$: C, 47.84; H, 3.68; N, 32.55. Found: C, 47.32; H, 3.84; N 33.40. The slight discrepancy in C and N data may be due to contamination with a small amount of precursor hydrazide.

L2. 2-Quinolinecarboxaldehyde (1.30 g, 8.27 mmol) was added to a slurry of pyridazine-3,6-dicarbohydrazide (0.78 g, 3.98 mmol; prepared from the reaction of 3,6-dicarbomethoxypyridazine[19] with hydrazine hydrate in MeOH) in MeOH (200 mL) and the mixture refluxed for 24 h. The resulting beige solid was then filtered, washed with diethyl ether (3 × 15 mL), and used without further purification. Yield: 1.78 g, 89.5%. Mp: 266−267 °C. MS (m/z): 475.2 (M + H). IR (ν/cm^{-1}): 1685 ($\nu_{C=O}$). ^{1}H NMR (500 MHz, DMSO-d_6, 25 °C): 13.08 (s, 2H, OH), 8.94 (d, $J = 31.43$ Hz, 2H, Ar), 8.30 (m, 10H, Ar), 7.83 (m, 2H, Ar), 7.67 (m, 2H). Anal. Calcd (%) for $C_{26}H_{18}N_8O_2 \cdot 1.4H_2O$ (bulk sample): C, 62.49; H, 4.20; N, 22.42. Found: C, 62.57; H, 4.19; N, 22.42.

$[Ni_4(L1)_4(H_2O)_4]$ (3). L1Me (0.05 g, 0.17 mmol) and $Ni(OAc)_2 \cdot 4H_2O$ (0.11 g, 0.43 mmol) were suspended in MeOH/MeCN (50:50, 20 mL), producing a dark-brown solution upon gentle heating. After 24 h, a small amount of light-brown precipitate formed, which readily dissolved upon the addition of 2 mL of water. A total of 18 drops (∼1 mL) of 0.82 M $NaBF_4$ (2:1 water/MeOH) were then added followed by 3 drops of 0.75 M NaOH(aq). The resulting solution was filtered and allowed to evaporate slowly. After 30 days, a small quantity (<5 mg) of red-brown platelike crystals formed, suitable for crystal structure determination. Magnetic data were collected on this uniform sample (vide infra). There was an insufficient sample for elemental analysis.

$[Ni_4(L1Me)_4(H_2O)_4](NO_3)_4 \cdot 8H_2O$ (4). L1Me (0.06 g, 0.20 mmol) and $Ni(NO_3)_2 \cdot 6H_2O$ (0.11 g, 0.45 mmol) were suspended in MeOH (20 mL), producing a light-brown solution upon warming. After 1 h, 5 drops of 0.75 M NaOH(aq) was added and the mixture heated at ∼50 °C for 12 h. The resulting solution was filtered, and slow evaporation for 14 days afforded a red-brown polycrystalline material. Yield: 20 mg, 21%. Anal. Calcd (%) for $(C_{12}H_{10}N_7O_3)_4Ni_4(H_2O)_4(NO_3)_4 \cdot 8H_2O$: C, 30.38; H, 3.37; N, 23.63. Found: C, 30.11; H, 2.97; N, 23.91.

$[Co_4(L1Me)_4(H_2O)_4](NO_3)_4 \cdot 11H_2O$ (5). L1Me (0.05 g, 0.17 mmol) and $Co(NO_3)_2 \cdot 6H_2O$ (0.11 g, 0.38 mmol) were suspended in 15 mL of MeOH, producing a red solution upon warming. After 5 min, 5 drops of 1 M NaOH(aq) was added and the mixture heated at ∼50 °C for 18 h. The resulting solution was then filtered, and slow evaporation for 28 days afforded red plates suitable for a structural determination. Yield: 20 mg, 25%. Anal. Calcd (%) for $(C_{12}H_{10}N_7O_3)_4Co_4(H_2O)_4(NO_3)_4 \cdot 11H_2O$: C, 29.48; H, 3.58; N, 22.93. Found: C, 29.59; H, 3.13; N, 22.80.

$[Co_9(2pmoap)_6](NO_3)_6 \cdot 24H_2O$ (8). 2pmoap[20] (0.12 g, 0.30 mmol) was added to a solution of $Co(NO_3)_2 \cdot 6H_2O$ (0.13 g, 0.45 mmol) in 20 mL of 1:1 MeOH/MeCN. The resulting orange-brown

(10) Tangoulis, V.; Raptopoulou, C. P.; Paschalidou, S.; Tsohos, A. E.; Bakalbassis, E. G.; Terzis, A.; Perlepes, S. P. *Inorg. Chem.* **1997**, *36*, 5270–5277.

(11) Ruben, M.; Rojo, J.; Romero-Salguero, F. J.; Uppadine, L. H.; Lehn, J.-M. *Angew. Chem., Int. Ed.* **2004**, *43*, 3644–3662.

(12) Dawe, L. N.; Abedin, T. S. M.; Thompson, L. K. *Dalton Trans.* **2008**, 1661–1675.

(13) Milway, V. A.; Abedin, S. M. T.; Niel, V.; Kelly, T. L.; Dawe, L. N.; Dey, S. K.; Thompson, D. W.; Miller, D. O.; Alam, M. S.; Müller, P.; Thompson, L. K. *Dalton Trans.* **2006**, 2835–2851.

(14) Dey, S. K.; Thompson, L. K.; Dawe, L. N. *Chem. Commun.* **2006**, 4947–4967.

(15) Dawe, L. N.; Thompson, L. K. *Angew. Chem., Int. Ed.* **2007**, *46*, 7440–7444.

(16) Dey, S. K.; Abedin, T. S. M.; Dawe, L. N.; Tandon, S. S.; Collins, J. L.; Thompson, L. K.; Postnikov, A. V.; Alam, M. S.; Müller, P. *Inorg. Chem.* **2007**, *46*, 7767–7781.

(17) Matthews, C. J.; Avery, K.; Xu, Z.; Thomspon, L. K.; Zhao, L.; Miller, D. O.; Biradha, K.; Poirier, K.; Zaworotko, M.; Wilson, C.; Goeta, A.; Howard, J. A. K. *Inorg. Chem.* **1999**, *38*, 5266–5276.

(18) Thompson, L. K.; Matthews, C. J.; Zhao, L.; Xu, Z.; Miller, D. O.; Wilson, C.; Leech, M. A.; Howard, J. A. K.; Heath, S. L.; Whittaker, A. G.; Winpenny, R. E. P. *J. Solid State Chem.* **2001**, *159*, 308–320.

(19) Sueur, S.; Lagrenee, M.; Abraham, F.; Bremard, C. *J. Heterocycl. Chem.* **1987**, *24*, 1285–1289.

(20) Dawe, L. N.; Abedin, T. S. M.; Kelly, T. L.; Thompson, L. K.; Miller, D. O.; Zhao, L.; Wilson, C.; Leech, M. A.; Howard, J. A. K. *J. Mater. Chem.* **2006**, *16*, 2645–2659.

solution was stirred with gentle heating for 3 h and then at room temperature for another 2 h. The resulting solution was filtered and the filtrate kept at room temperature for crystallization. A red-brown crystalline solid formed after 13 days, which was recrystallized from CH_3OH/CH_3CN (1:1) to give red prismatic crystals, suitable for X-ray diffraction. Yield: 0.15 g, 67%. Anal. Calcd (%) for $[(C_{17}H_{13}N_{11}O_2)_6Co_9](NO_3)_6 \cdot 24H_2O$: C, 32.63; H, 3.38; N, 26.89. Found: C, 32.06; H, 2.77; N 27.43.

$[(2pmoap\text{-}2H)_6Mn_5Zn_4](NO_3)_6 \cdot 33H_2O \cdot 20CH_3OH$ (14). 2pmoap[20] (0.15 g, 0.31 mmol) was added to a solution of $Mn(NO_3)_2 \cdot 6H_2O$ (0.13 g, 0.45 mmol) in MeOH/MeCN (15 mL:5 mL), forming a clear, light-yellow solution. $Zn(CH_3COO)_2 \cdot 2H_2O$ (0.060 g, 0.27 mmol) was added, and the solution became clear and orange. It was stirred with gentle heating for 30 min and then kept after filtration for slow evaporation. Orange, prismatic crystals, suitable for a crystallographic study, were collected after 6 days. Yield: 0.023 g, 7.5%. Anal. Calcd (%) for $[(C_{17}H_{13}N_{11}O_2)_6Mn_5Zn_4](NO_3)_6(H_2O)_{33}(CH_3OH)_{20}$: C, 32.11; H, 4.95; N, 22.10. Found: C, 32.20; H, 2.83; N, 22.02.

$[(2pmoap\text{-}2H)_6Mn_5Cu_4](NO_3)_6 \cdot 15H_2O \cdot 2CH_3OH$ (16). $[Mn_9(2pmoap\text{-}2H)_6](NO_3)_6 \cdot 28H_2O$ (**15**)[20] (0.12 g, 0.034 mmol) was dissolved in MeOH/MeCN (7 mL:7 mL) to give a clear dark-orange solution, which was treated with 0.1 M NaOH(aq) until a neutral pH was achieved. A solution of $Cu(NO_3)_2 \cdot 6H_2O$ (0.050 g, 0.17 mmol) dissolved in methanol/acetonitrile (5 mL:5 mL) was added to give a clear brown solution. The pH was tested, and four drops of triethylamine was added to maintain a neutral pH. The solution was stirred with gentle heating for 1 h and then filtered. Crystals suitable for X-ray analysis formed in 6 days. Yield: 0.03 g, 24%. Anal. Calcd (%) for $[(C_{17}H_{13}N_{11}O_2)_6Mn_5Cu_4](NO_3)_6(H_2O)_{15}(CH_3OH)_2$: C, 34.17; H, 3.19; N, 27.59. Found: C, 34.15; H, 2.47; N, 27.64.

$[(2pmoap\text{-}2H)_6Mn_1Cu_8](NO_3)_6 \cdot 23H_2O$ (18). $Cu(NO_3)_2 \cdot 6H_2O$ (0.10 g, 0.34 mmol) was added to a solution of $[Mn_9(2pmoap\text{-}2H)_6](NO_3)_6 \cdot 28H_2O$[20] (0.050 g, 0.014 mmol) in MeOH/MeCN (5 mL:5 mL) to give a clear green-brown solution that was gently refluxed for 1 h and kept after filtration for slow evaporation. Brown, prismatic crystals suitable for a crystallographic study were collected after 13 days. Yield: 0.020 g, 38%. Anal. Calcd (%) for $[(C_{17}H_{13}N_{11}O_2)_6Mn_1Cu_8](NO_3)_6(H_2O)_{23}$: C, 32.50; H, 3.32; N, 26.75. Found: C, 32.04; H, 2.52; N, 27.29.

$[(L2\text{-}2H)_8Mn_{16}(O)_4(OH)_4](NO_3)_4 \cdot 42H_2O \cdot 4CH_3CN$ (19). $Mn(NO_3)_2 \cdot 6H_2O$ (0.21 g, 0.73 mmol) was added to a beige slurry of L2 (0.11 g, 0.22 mmol) in 1:1 CH_3CN/CH_3OH (20 mL). NaOH(aq) (1 mL of 1.17 M; ∼1 mmol) was added in order to achieve a neutral pH, turning the reaction mixture cloudy and brown. Upon the addition of 5 mL of H_2O, the solution became clear and brown. The solution was heated gently (∼55 °C) for 20 h, with a change in color to red, and then filtered. The dark-red filtrate was preserved for crystallization. Red crystals, suitable for X-ray analysis, formed upon standing for 3 days. Yield: 0.060 g, 38%. Anal. Calcd (%) for $[(C_{26}H_{16}O_2N_8)_8Mn_{16}(O)_4(OH)_4](NO_3)_4(H_2O)_{42}(CH_3CN)_4$: C, 43.53; H, 3.85; N, 16.94. Found (bulk sample) (%): C, 43.24; H, 3.11; N, 17.37.

$[Cu^{II}_{12}Cu^{I}_4(L5)_8](CF_3SO_3)_{12} \cdot 24H_2O$ (21). L5[15] (0.12 g, 0.30 mmol) was added to a solution of $Cu(CF_3SO_3)_2$ (0.22 g, 0.61 mmol) in 1:1 CH_3OH/CH_3CN (20 mL). The resulting dark-green solution was stirred with gentle heating for 18 h. A solution of $KAg(CN)_2$ (0.06 g, 0.3 mmol) in 1:1 CH_3OH/H_2O (5 mL) was then added dropwise over 2 min, changing the solution to a clear dark-brown color. This solution was heated gently (∼50 °C) for 48 h, cooled to room temperature, and filtered. Brown needlelike crystals, suitable for X-ray diffraction, formed upon standing for 4 days. Yield: 0.090 g, 38%. Anal. Calcd (%) for $[(C_{16}H_{12}N_{12}O_2)_8Cu_{16}](CF_3SO_3)_{12}(H_2O)_{24}$: C, 26.00; H, 2.24; N, 20.77. Found: C, 26.20; H, 1.76; N, 20.65.

Results and Discussion

Homovalent Homometallic Grids. [2 × 2] Grids. The reaction between the ligand and the metal ion is built upon the complementary nature of the coordination environment provided by the ligand and the "coordination algorithm" of the metal ion, which expresses its most comfortable geometry and ligand donor complement. With typically six-coordinate metal ions if the ligand coordination pocket can provide a *mer* tridentate donor grouping with the formation of five-membered chelate rings, then the directional influence of an octahedral metal will act as a 90° pivot about which the grid will grow in a 2-D square grid arrangement (Scheme 1 illustrates the [2 × 2] and [3 × 3] cases).

Hydrazones have been a powerful group of ligands for this type of self-assembly, with the simplicity of the RC═ONHNHR′ entity providing the focus for bridged aggregates via μ-O or μ-NN linkages. Terminating or linking heterocyclic groups (R and R′) provide complementary donors to fulfill the *mer*-coordination spheres at the metal centers. Simple ditopic ligands, e.g., poap and pomp (Chart 1), produce [2 × 2] $[M_4(\mu\text{-}O)_4]$ square grids in which the deprotonated hydrazone oxygen atom bridges the metal ions (M = Mn, Co, Ni, Cu, Zn).[17,18] Because the ligands only fill five coordination positions, with six-coordinate metal ions, extra ligands, e.g., solvent and anion, are also coordinated at some sites. Figure 1 illustrates a typical heteroleptic Mn^{II} grid example, $[Mn_4(poap)_4(N_3)_4]$ (**1**),[20] which exhibits antiferromagnetic exchange ($J = -3.1$ cm^{-1}), based on the isotropic exchange Hamiltonian (eq 1; $S = {}^5/_2$).

Scheme 1

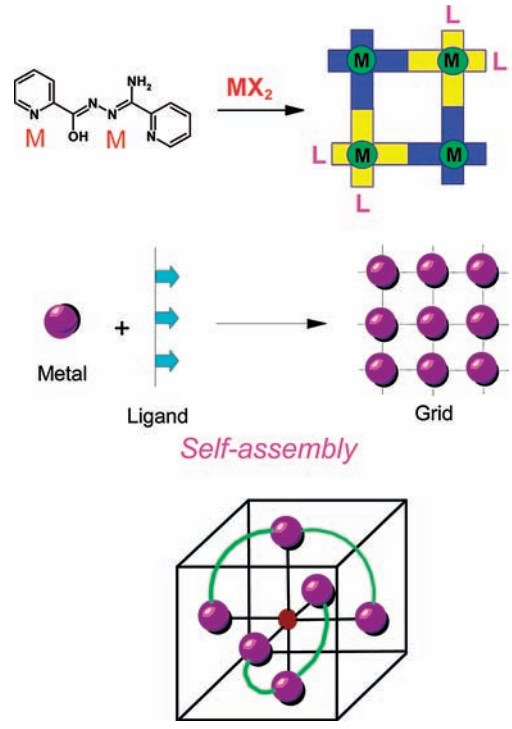

$$H_{ex} = -J\{S_1 \cdot S_2 + S_2 \cdot S_3 + S_3 \cdot S_4 + S_1 \cdot S_4\} \quad (1)$$

The large Mn−O−Mn bridge angles (128−131°) lead to the antiferromagnetic exchange coupling. In the absence of the competitive coordination effect of the anion and solvent, homoleptic pentanuclear clusters result, e.g., $[Mn_5(poap)_6](ClO_4)_4$ (**2**) (Figure 2).[21] This highlights the power of the encoded coordination information in the ligand because it is maximized in the homoleptic cluster formation.[22] Intracluster Mn−Mn exchange via Mn−O−Mn interactions again leads to antiferromagnetic behavior ($J = -1.5$ cm^{-1}). Pentanuclear Co^{II} and Zn^{II} clusters are also formed.[22]

The basic construction element of the polynucleating ditopic hydrazone ligands can be modified to include a variety of heterocyclic monodentate terminating groups, resulting in slightly different [2 × 2] complexes. The incorporation of potentially polynucleating end pieces, e.g., pyridazine, carboxylate, and pyrazine in L1 (Chart 1), presents an interacting metal ion with additional coordination possibilities and the potential for greatly expanded nuclearity and even extended long-range coordination. However, the metal ion coordination algorithm must also be considered in terms of a potential outcome. This ligand forms simple [2 × 2] square grids with Co^{II} and Ni^{II} in which the familiar core $[M_4(\mu\text{-}O)_4]$ structure occurs. The reaction of the methyl ester of L1 with $Ni(CH_3COO)_2$ gave a small quantity of red-brown crystals (**3**) suitable for a structural determination

Chart 1

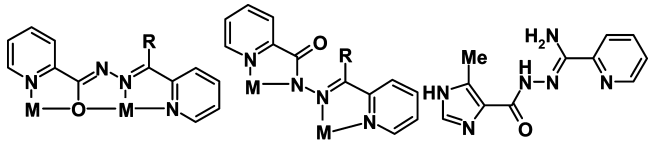

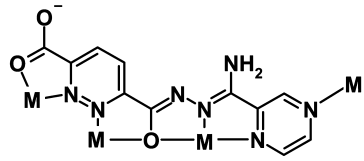

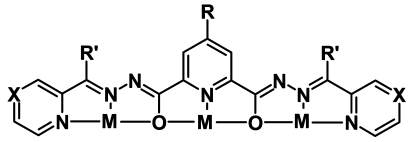

2poap(R=H,R'=NH2,X=CH),Cl2poap(R=Cl,R'=NH2,X=CH),
2pomp(R=H,R'=CH3,X=CH),S2poap(R=SH,R'=NH2,X=CH),
2poapz(R=H,R'=NH2,X=N),2popp(R=H,R'=Ph,X=CH),
Cl2popp (R=Cl,X=CH,R'=Ph)

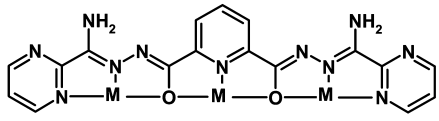

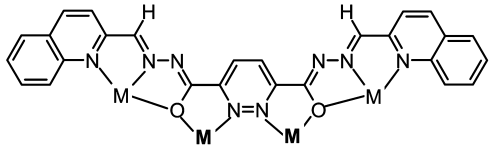

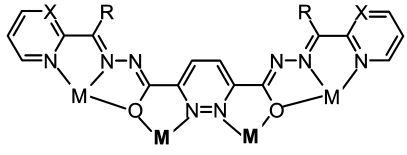

L3 (R=NH2,X=CH),L4 (R=H,X=CH),L5 (R=NH2,X=N)

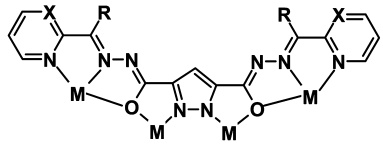

L6 (R=H,X=CH),L7 (R=NH2,X=N)

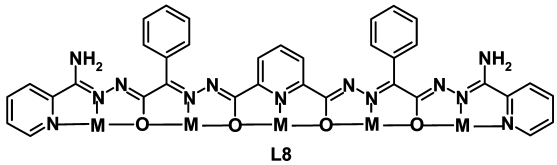

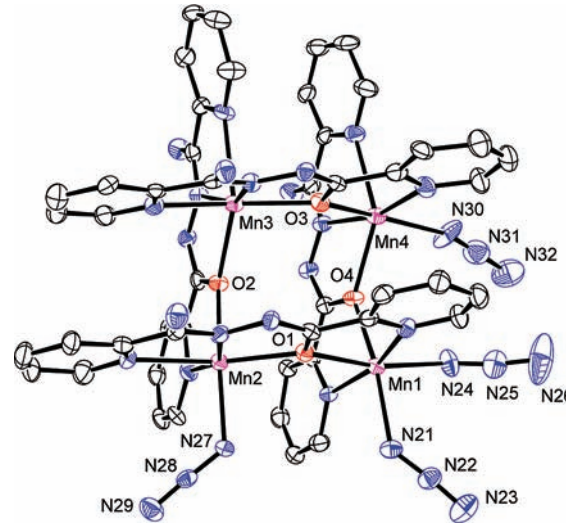

Figure 1. ORTEP structural representation of **1**.

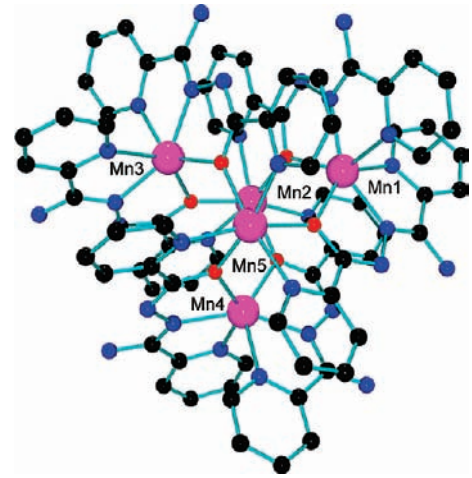

Figure 2. POVRAY structural representation of the cation in **2**.

Table 1. Summary of Crystallographic Data for **3**, **5**, **8**, **14**, **16**, **19**, and **21**

	3	**5**	**8**
chemical formula	$C_{53.2}H_{72.8}Ni_4N_{28}O_{25.2}$	$C_{49.5}H_{72.5}Co_4N_{32}O_{38.75}$	$C_{106}H_{06}Co_9\ N_{74}O_{41}$
M	1742.53	1971.54	3602.87
T (K)	153(2)	153(2)	153(2)
cryst syst	monoclinic	triclinic	orthorhombic
space group	*C*2/*c* (No. 15)	$P\bar{1}$ (No. 2)	*Fddd* (No. 70)
a (Å)	29.508(4)	13.182(2)	39.369(3)
b (Å)	16.6429(18)	15.536(3)	39.416(3)
c (Å)	16.857(2)	22.573(3)	39.411(3)
α (deg)	90.00	103.9946(9)	90.00
β (deg)	113.239(2)	94.291(2)	90.00
γ (deg)	90.00	115.018(3)	90.00
V (Å^3)	7606.8(16)	3981.5(10)	61157(8)
Z	4	2	16
D_{calcd} (g/cm^3)	1.521	1.644	1.565
μ(Mo Kα) (cm^{-1})	10.68	9.32	10.51
reflns total	32 733	33 863	133 536
reflns unique	7881	16 309	15 853
R_{int}	0.0434	0.0510	0.0415
R1 [$I > 2.00\sigma(I)$]	0.0597	0.0914	0.0988
wR2 (all reflns)	0.1866	0.2343	0.2877

	14	**16**	**19**	**21**
chemical formula	$C_{102}H_{106}Mn_5N_{72}O_{42}Zn_4$	$C_{102}H_{126}Cu_4Mn_5N_{72}O_{54}$	$C_{208}H_{196}Mn_{16}N_{68}O_{68}$	$C_{140}H_{101.6}Cu_{16}F_{36}N_{96}O_{54.8}S_{12}$
M	3548.63	3753.44	5615.26	6090.75
T (K)	153(2)	153(2)	153(2)	153(2)
cryst syst	tetragonal	tetragonal	tetragonal	tetragonal
space group	$I4_1/acd$ (No. 142)	$I4_1/acd$ (No. 142)	$P\bar{4}2_1c$ (No. 114)	$P4_2/n$ (No. 86)
a (Å)	27.958(3)	27.6101(16)	22.856(2)	23.579(3)
b (Å)	27.958(3)	27.6101(16)		
c (Å)	39.801(4)	40.319(2)	27.634(3)	22.196(2)
α (deg)	90.00	90.00	90.00	90.00
β (deg)	90.00	90.00	90.00	90.00
γ (deg)	90.00	90.00	90.00	90.00
V (Å^3)	31112(5)	30736(3)	14436(2)	12341(2)
Z	8	8	2	2
D_{calcd} (g/cm^3)	1.515	1.622	1.292	1.639
μ(Mo Kα) (cm^{-1})	10.94	10.47	7.53	15.63
reflns total	96366	65432	114457	26597
reflns unique	7665	7972	14185	11965
R_{int}	0.0992	0.0386	0.0574	0.0335
R1 [$I > 2.00\sigma(I)$]	0.1168	0.0812	0.0934	0.1133
wR2 (all reflns)	0.2855	0.2378	0.2706	0.3400

(Table 1). The structure of the neutral complex **3** is shown in Figure 3, and important bond distances and angles are listed in Table 2. The Ni_4 square core is shown in Figure 4. The ligand found in the complex is, in fact, the carboxylic acid (L1), which is clearly obtained as a result of hydrolysis of the ester form during reaction with the metal salt. The complex has the familiar [2 × 2] square structure with four six-coordinate Ni^{II} ions bridged by four deprotonated hydrazone oxygen atoms with a Ni−O−Ni bridge angle of

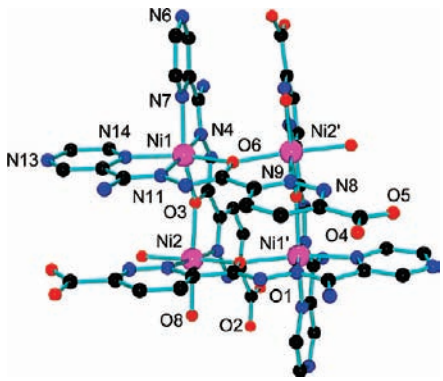

Figure 3. POVRAY structural representation of the cation in **3**.

Table 2. Bond Distances (Å) and Angles (deg) for **3**

Ni1−N11	1.959(2)	Ni2−O8	2.066(3)
Ni1−N4	1.965(2)	Ni2−O6	2.0663(19)
Ni1−N7	2.114(3)	Ni2−N9	2.071(2)
Ni1−O6	2.1212(19)	Ni2−O3	2.072(2)
Ni1−N14	2.124(3)	Ni2−N2	2.080(2)
Ni1−O3	2.129(2)	Ni2−O7	2.082(2)
Ni2−O6−Ni1	138.09(10)		

138.09(10)°. Ni−L bond distances fall in the range 1.959−2.129 Å, typical of Ni^{II}_4 square grids in this class.[18] The reaction of L1Me with $Ni(NO_3)_2$ gave the brown complex **4** (see the Experimental Section) in which the ligands appear to be present in their ester form.

A comparable Co^{II}_4 grid complex **5** forms from the reaction of L1Me with cobalt nitrate and again retains the ester form of the ligand. Figure 5 shows the structure of the cation, and the core structure is shown in Figure 6. Important bond distances and angles are listed in Table 3. Co−L distances fall in the range 1.996−2.222 Å, typical of Co^{II} in [2 × 2] grids, and the large Co−O−Co angles (132.7−134.6°) would suggest antiferromagnetic exchange (vide infra).[18] Despite the availability of several other donor options, Ni^{II} and Co^{II}

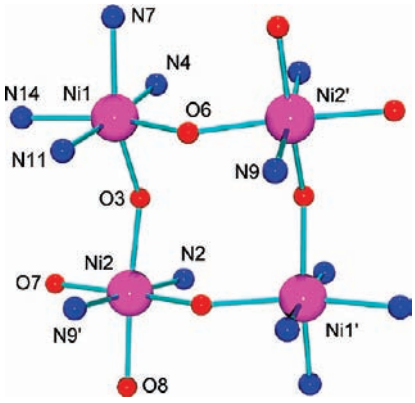

Figure 4. POVRAY structural representation of the core structure in **3**.

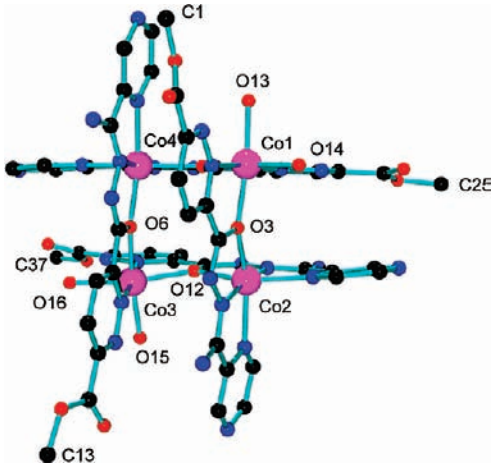

Figure 5. POVRAY structural representation of the cation in **5**.

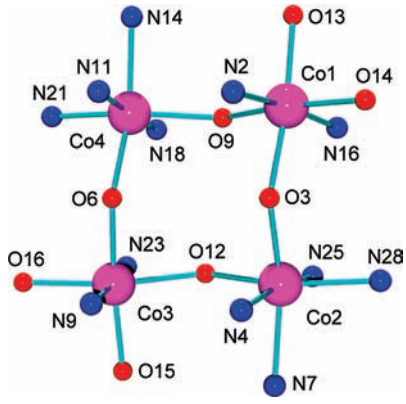

Figure 6. POVRAY structural representation of the core structure in **5**.

stick to the familiar [2 × 2] grid motif based on the typical ditopic ligand pocket arrangement.

The magnetic behavior of complexes **3**−**5** is similar, with maxima in χ_{mol} at low temperatures, indicative of intramolecular antiferromagnetic exchange. Figure 7 shows the profile of χ_{mol} as a function of the temperature for **4**, with a maximum in χ_{mol} at ∼30 K, typical of a [2 × 2] square antiferromagnetic grid. The magnetic moment per mole drops from 6.4 μ_B at 300 K to 1.0 μ_B at 2 K. A successful fit of the data to an exchange equation derived from eq 1 (S = 2/2) gave $g = 2.231(1)$, $J = -14.2(1)$ cm^{-1}, TIP = 1150 × 10^{-6} cm^{-1} mol^{-1}, $\rho = 0.027$ ($10^2R = 1.9$; $R = [\sum(\chi_{obsd} - \chi_{calcd})^2/\sum\chi_{obsd}^2]^{1/2}$) (TIP = temperature-independent paramagnetism, ρ = fraction of paramagnetic impurity; solid line in Figure 7). Variable-temperature magnetic data were obtained on a very small sample of **3** (<1 mg) with a similar maximum in χ_m at 30 K. A comparable data fit for **3** gave $J = -14.7$ cm^{-1}. The antiferromagnetic exchange is associated with the large Ni−O−Ni bridge angles.[17] **5** shows a drop in the magnetic moment per mole from 9.26 μ_B at 300 K to 3.55 μ_B at 2 K (Figure 8). Fitting of the data to eq 1 (S = 3/2) gave $g = 2.40(2)$, $J = -4.0(2)$ cm^{-1}, TIP = 1380 × 10^{-6} cm^3 mol^{-1}, $\rho = 0.029$ ($10^2R = 5.3$; solid line in Figure 8). This is an isotropic spin-only fit, which would perhaps be considered inappropriate for Co^{II} given the potential population of $S = {}^1/_2$ states at low temperature, and single-ion anisotropy effects, which would bias the data somewhat. Some measure of the single-ion effect can be observed by examining the magnetic properties of Co^{II}/Co^{III} complexes

Table 3. Bond Distances (Å) and Angles (deg) for **5**

Co1−O14	2.060(4)	Co3−O16	2.064(4)
Co1−O13	2.063(5)	Co3−O15	2.070(5)
Co1−O9	2.066(4)	Co3−O6	2.095(4)
Co1−O3	2.091(4)	Co3−O12	2.097(4)
Co1−N16	2.122(5)	Co3−N23	2.115(5)
Co1−N2	2.146(5)	Co3−N9	2.131(5)
Co2−N25	1.996(5)	Co4−N18	2.003(5)
Co2−N4	2.017(5)	Co4−N11	2.007(5)
Co2−O12	2.129(4)	Co4−O9	2.109(4)
Co2−O3	2.150(4)	Co4−O6	2.118(4)
Co2−N28	2.184(5)	Co4−N21	2.159(5)
Co2−N7	2.222(5)	Co4−N14	2.162(5)
Co1−O3−Co2	134.6(2)	Co1−O9−Co4	132.7(2)
Co3−O6−Co4	133.88(19)	Co3−O12−Co2	133.0(2)

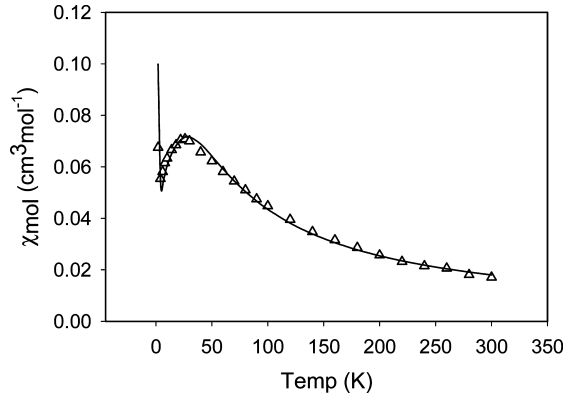

Figure 7. Variable-temperature magnetic properties of **4** (see the text for fitted parameters).

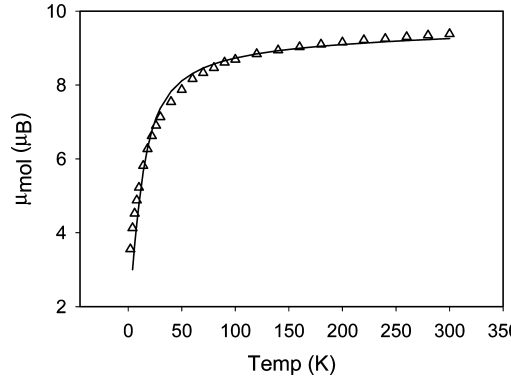

Figure 8. Variable-temperature magnetic properties of **5** (see the text for fitted parameters).

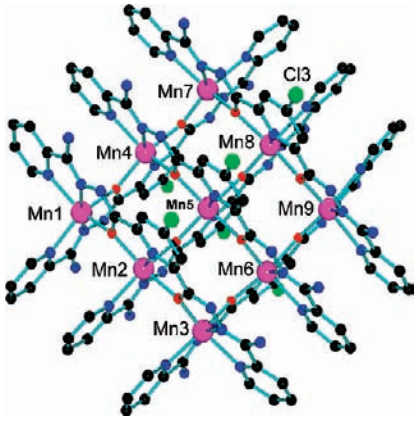

Figure 9. POVRAY structural representation of the cation in **6**.

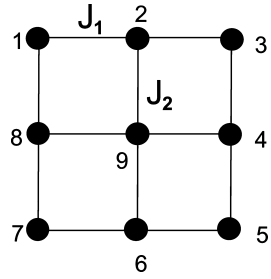

Figure 10. Magnetic exchange model for a [3 × 3] grid.

with comparable ligands. The dinuclear Co^{III}/Co^{II} complex $[(ioap)_2Co_2(H_2O)_4](BF_4)_2$ (ioap; Chart 1) is of direct relevance and has the single Co^{II} center in a bidentate N_2 pocket of the related ligand ioap, with a N_2O_4 coordination sphere.[23] The magnetic moment of this compound shows a small drop in the magnetic moment from 4.5 μ_B at 300 K to 3.4 μ_B at 2 K. This would scale up to 9.0 μ_B to 6.8 μ_B for a putative Co^{II}_4 grid with no exchange in the same temperature range. It is clear, therefore, that antiferromagnetic exchange is a very significant component of the magnetic properties of **5**. Zero-field splitting for Ni^{II} might also be considered as a complicating contribution to the understanding of bulk magnetic properties, but theoretical calculations show that for even quite substantial $|D|$ values (e.g., 5−10 cm^{-1}) no maximum in χ is observed above 5 K. The Ni^{II} magnetic properties are therefore dominated by exchange effects.

[3 × 3] Grids. Extending the basic ligand structure to increased polytopic order can be effected easily by using bis-hydrazone precursors. 2poap and related ligands (Chart 1) are built on a central pyridine-2,6-bis-hydrazone core, which can be terminated with a variety of donor end groups to create tritopic ligands. In the typical tritopic μ-$O_{hydrazone}$ coordination mode (Chart 1), they readily incorporate three metal ions with the formation of five-membered chelate rings and with the donors arranged in a *mer* fashion with respect to each metal ion. The *mer* coordination of three contiguous metal ions predisposes this subunit to the formation of a [3 × 3] grid (Scheme 1) by the sequential organization of similar subunits with a 90° orientation. Some discussion of the possible mechanism of such an assembly has already been published,[12] resulting from an analysis of lower nuclearity intermediates, which have been isolated and characterized structurally.[24,25] The complex $[Mn_9(Cl2poap)_6](ClO_4)_6$ (**6**) (Figure 9) is a typical example, with nine Mn^{II} centers held in close proximity by μ-$O_{hydrazone}$ linkages within the compact [3 × 3] grid, held in place by the six ligands. Mn−Mn separations fall in the range 3.94−4.03 Å with Mn−O−Mn angles of 126−131°.[26] Mn_9 grids in this class all exhibit intramolecular antiferromagentic exchange, with typical J values of ∼−5 cm^{-1}.[26] The exchange model (Figure 10) includes two J values (J_1 in the outer ring of eight metal ions and J_2 involving the central metal and its immediate neighbors). Using the full exchange Hamiltonian (eq 2) results in enormous matrix calculations.

$$H_{ex} = -J_1\{S_1\cdot S_2 + S_2\cdot S_3 + S_3\cdot S_4 + S_4\cdot S_5 + S_5\cdot S_6 + S_6\cdot S_7 + S_7\cdot S_8 + S_1\cdot S_8\} - J_2\{S_2\cdot S_9 + S_4\cdot S_9 + S_6\cdot S_9 + S_8\cdot S_9\} \quad (2)$$

$$\chi_{Mn} = \frac{Ng^2\beta^2 S(S+1)}{3kT}\,\frac{1+u}{1-u} \quad (3)$$

$$u = \coth\left[\frac{JS(S+1)}{kT}\right] - \left[\frac{kT}{JS(S+1)}\right] \quad (4)$$

$$\chi_{mol} = [(8\chi_{Mn} + 1.094g^2)/(T-\theta)](1-\rho) + (1.094g^2/T)\rho + \mathrm{TIP} \quad (5)$$

For the Mn^{II}_9 case, this 45-electron problem cannot be dealt with directly because the largest matrix dimension is 88 900, requiring approximately 60 GB of computer RAM, clearly beyond the capacity of most computers. Calculations on lower order systems are easier, but for $(d^4)_9$ (largest dimension 25 200 requiring 5.1 GB), problems still arise. A lengthy discussion on this issue has been published.[27] In the case of Mn^{II}_9, a simplification involved setting $J = J_1$ and $J_2 = 0$, which was considered reasonable on the basis of the similar Mn−O−Mn bridge angles throughout the grid. Also, because the antiferromagnetic ground state is $S' = {}^5/_2$, as a result of the odd number of spin centers, the outer ring of eight metal ions can effectively be separated from the central metal and treated as a chain. The assumption that J_2 is effectively zero in reality will not be true but serves to greatly simplify the modeling of the exchange problem. The chain model based on the Fisher approach is given in eqs 3−5, which account also for the central metal ion, and other corrective terms (TIP = temperature-independent paramagnetism, θ = Weiss correction, and paramagnetic impurity fraction). Good data

(21) Matthews, C. J.; Xu, Z.; Mandal, S. K.; Thompson, L. K.; Biradha, K.; Poirier, K.; Zaworotko, M. J. *Chem. Commun.* **1999**, 347–348.
(22) Matthews, C. J.; Thompson, L. K.; Parsons, S. R.; Xu, Z.; Miller, D. O.; Heath, S. L. *Inorg. Chem.* **2001**, *40*, 4448–4454.
(23) Dawe, L. N.; Thompson, L. K. *Dalton Trans.* **2008**, 3610–3618.
(24) Thompson, L. K.; Matthews, C. J.; Zhao, L.; Wilson, C.; Leech, M. A.; Howard, J. A. K. *Dalton Trans* **2001**, 2258–2262.
(25) Niel, V.; Milway, V. A.; Dawe, L. N.; Grove, H.; Tandon, S. S.; Abedin, T. S. M.; Kelly, T. L.; Spencer, E. C.; Howard, J. A. K.; Collins, J. L.; Miller, D. O.; Thompson, L. K. *Inorg. Chem.* **2008**, *47*, 176–189.
(26) Thompson, L. K.; Zhao, L.; Xu, Z.; Reiff, W. M. *Inorg. Chem.* **2003**, *42*, 128–139.
(27) Zhao, L.; Xu, Z.; Grove, H.; Milway, V. A.; Dawe, L. N.; Abedin, T. S. M.; Thompson, L. K.; Kelly, T. L.; Harvey, R. G.; Miller, D. O.; Weeks, L.; Shapter, J. G.; Pope, K. J. *Inorg. Chem.* **2004**, *43*, 3812–3824.

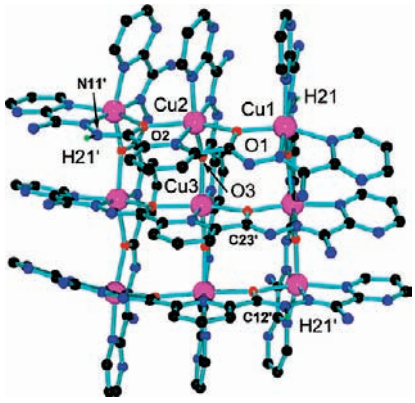

Figure 11. POVRAY structural representation of the cation in **7**.

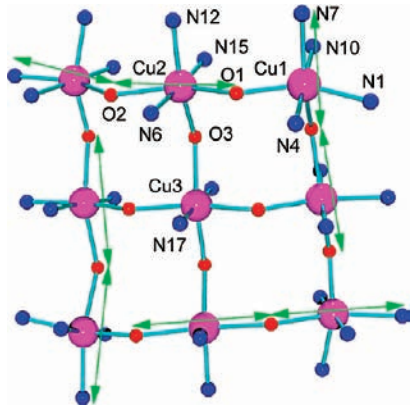

Figure 12. POVRAY structural representation of the core in **7** (arrows indicate the Jahn−Teller axes).

fits can be obtained in most cases with J values of ∼−5 cm^{-1}.[20,25−28]

Cu^{II}_9 [3 × 3] grids form readily with the same structural arrangement. Figure 11 shows a typical example, e.g., $[Cu_9(2pmoap)_6](ClO_4)_{10}$ (**7**), with the nine six-coordinate Cu^{II} ions connected by μ-$O_{hydrazone}$ bridges (Cu−O−Cu 136−143°).[20] Figure 12 shows the core structure, in which the Jahn−Teller axes of the axially elongated ($d_{x^2-y^2}$ magnetic ground state) copper ions in the outer Cu_8 ring are highlighted. This creates a situation where magnetically orthogonal connections exist between these copper ions, leading to the absence of antiferromagnetic exchange. However, the central copper is axially compressed (d_{z^2} ground state), leading to antiferromagnetic exchange with its neighbors. Using eq 2 within the software package *MAGMUN4.1*,[29] the variable-temperature magnetic data gave a reasonable fit for $g = 2.28$, $J_1 = 0.35$ cm^{-1}, $J_2 = -35$ cm^{-1}, and TIP = 800 × 10^{-6} cm^3mol^{-1}. The ferromagnetic exchange in the outer ring is consistent with the orthogonal nature of the bridges, while the antiferromagnetic term also is consistent with the nonorthogonal connection between the central copper ion and its neighbors.[20]

Magnetic [3 × 3] grids with other first-row transition-metal ions have proved difficult to synthesize. In the case of Co^{II}, this has been complicated by the susceptibility of the systems to undergo partial oxidation of Co^{II} to Co^{III},[18,23,25] and in the case of nickel a reluctance to form full grids.[25] The balance of effects controlling complex formation includes many contributing factors, and this has been discussed at some length,[12] but with cobalt and nickel, the most likely critical barrier to grid formation involves the crystal-field stabilization energy (CFSE) effects associated with the metal salts used in the syntheses. However, the red crystalline complex **8** was obtained from a CH_3CN/MeOH solution, suitable for structural analysis, and is reported herein. Abbreviated crystal data are given in Table 1, and important distances and angles are listed in Table 4. The structure of the nonanuclear cation in **8** is shown in Figure 13 and the core structure involving just the immediate donor atoms in Figure 14. The complex has a typical [3 × 3] μ-O-bridged grid structure, with the nine six-coordinate metal ions embedded within the assembly of two roughly parallel groups of three ligands above and below the metal pseudoplane. Co−N distances fall in the range 2.009−2.217 Å and Co−O distances in the range 2.119−2.190 Å. Bond valence sum (BVS) values fall in the range 2.17−2.37, typical of Co^{II} with this type of ligand.[18,25,30] Co−O−Co angles fall in the typical range 135.1−136.3°, and Co−Co separations fall in the range 3.960−4.038 Å.

Table 4. Bond Distances (Å) and Angles (deg) for **8**

Co1−N21	2.010(5)	Co3−N28	2.125(5)
Co1−N4	2.011(5)	Co3−O5	2.178(4)
Co1−O4	2.120(4)	Co3−N11	2.217(5)
Co1−N1	2.127(5)	Co4−N15	2.009(5)
Co1−O1	2.177(4)	Co4−N23	2.041(5)
Co1−N18	2.213(5)	Co4−O3	2.126(4)
Co2−N32	2.004(5)	Co4−O4	2.163(4)
Co2−N6	2.045(5)	Co4−O5	2.190(4)
Co2−O6	2.123(4)	Co4−N12	2.212(6)
Co2−O2	2.162(4)	Co5−N34	2.020(7)
Co2−O1	2.188(4)	Co5−N17	2.029(7)
Co2−N29	2.213(6)	Co5−O3	2.150(4)
Co3−N25	2.009(5)	Co5−O3	2.151(4)
Co3−N8	2.011(5)	Co5−O6	2.154(4)
Co3−O2	2.119(4)	Co5−O6	2.155(4)
Co1−O1−Co2	135.3(2)	Co1−O4−Co4	135.22(19)
Co3−O2−Co2	135.36(19)	Co3−O5−Co4	135.13(19)
Co4−O3−Co5	136.3(2)	Co2−O6−Co5	136.3(2)

The proximity of the Co^{II} ions in the closely packed Co_9 square grid structure, with μ-O as bridges, suggests that the magnetic properties should be dominated by intramolecular antiferromagnetic exchange. The variable-temperature mag-

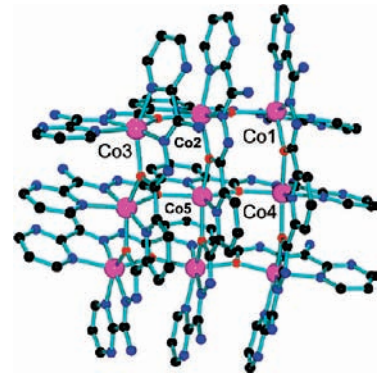

Figure 13. POVRAY structural representation of the cation in **8**.

(28) Thompson, L. K.; Waldmann, O.; Xu, Z. *Coord. Chem. Rev.* **2005**, *249*, 2677–2690.

(29) MAGMUN4.1/OW01.exe is available as a combined package free of charge from the authors (http://www.ucs.mun.ca/∼lthomp/magmun). MAGMUN has been developed by Dr. Zhiqiang Xu (Memorial University) and OW01.exe by Dr. O. Waldmann.

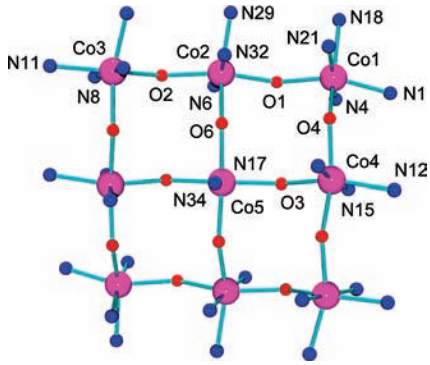

Figure 14. POVRAY structural representation of the core in **8**.

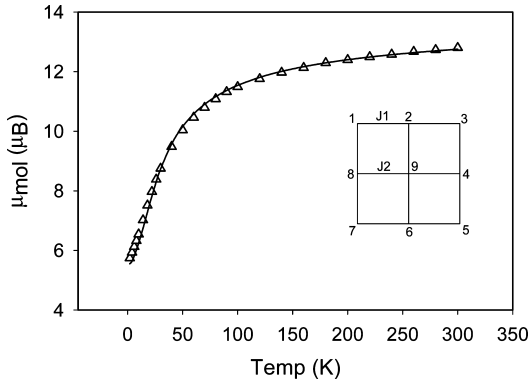

Figure 15. Variable-temperature magnetic properties of **8** (see the text for fitted parameters).

netic properties of **8** are shown in Figure 15, as a plot of the magnetic moment (per mole) as a function of the temperature. The room temperature magnetic moment (12.8 μ_B; 4.3 μ_B per metal) is consistent with nine high-spin Co^{II} centers in an antiferromagnetically coupled [3 × 3] grid. The residual magnetic moment (5.7 μ_B) at 2 K is slightly larger than expected for a single Co^{II} ion anticipated in the ground state. Using a simple isotropic exchange model for nine $S = {}^3/_2$ spin centers and one J value (eq 2; Figure 10; $J = J_1 = J_2$), the exchange was modeled successfully using *MAGMUN4.1*[29] to give $g = 2.263(9)$, $J = -6.5(2)$ cm^{-1}, TIP = 2200×10^{-6} cm^3 mol^{-1}, $\rho = 0.075$. The fitted J value compares closely with those obtained for [2 × 2] Co^{II}_4 grids with closely related ditopic hydrazone ligands and comparable Co−O−Co bridge angles (e.g., $J = -6.9$ cm^{-1}).[18] Again this model does not account for possible ground-state contributions from $S = {}^1/_2$ states associated with Kramer's doublet terms, but the J value is entirely consistent with exchange energies associated with comparable μ-O-bridged Mn^{II}_9 [3 × 3] grid complexes.[25−28] On the basis of the comparison with $[(ioap)_2Co_2(H_2O)_4](BF_4)_2$ (vide supra), this would translate to a range of 13.5 μ_B at 300 K to 10.2 μ_B at 2 K for a putative [3 × 3] grid with nine comparable uncoupled Co^{II} ions. This indicates that the much more dramatic drop in the magnetic moment for **8** is clearly strongly influenced by intramolecular antiferromagnetic exchange.

(30) (a) Palenik, G. J. *Inorg. Chem.* **1997**, *36*, 122. (b) O'Keefe, M.; Brese, N. E. *J. Am. Chem. Soc.* **1991**, *113*, 3226.

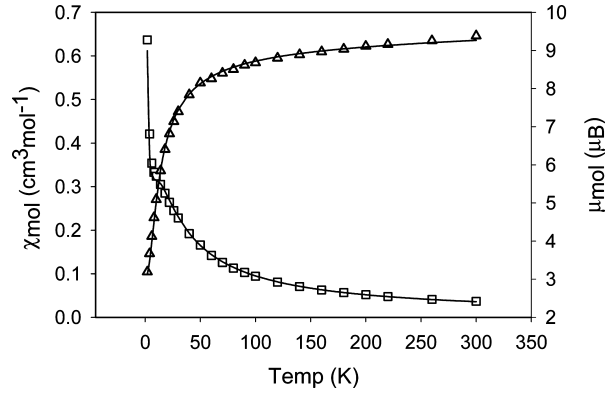

Figure 16. Variable-temperature magnetic properties of **9** (see the text for fitted parameters).

The synthesis and characterization of a full $[Ni_9L_6]$ [3 × 3] grid has so far not been successful, and only partial grids have been produced with Ni^{II}.[25] However, the [3 × 3] grid based complex $[Ni_9(Cl2popp)_5(OH)_2(CH_3CN_2)_2(H_2O)_3](ClO_4)_6$ (**9**) has been synthesized and structurally characterized, although at this time details are not publishable because of poor refinement.[25] The expected $[Ni_9(\mu\text{-}O)_{12}]$ core exists, but the lack of one central ligand leads to the involvement of μ-OH bridges in place of the typical hydrazone oxygen bridges. Magnetically this does not change the exchange picture, and large Ni−O−Ni bridge angles lead to the expected antiferromagnetic behavior. Variable-temperature magnetic data (Figure 16) show a shoulder in the χ_M profile, typical of an antiferromagnetic system, with a sharp rise at lower temperature, consistent with an odd number of metal centers. The magnetic moment drops smoothly from 9.4 μ_B at 300 K to 3.2 μ_B at 2 K, again indicating intramolecular antiferromagnetic exchange, with a ground state consistent with one residual Ni^{II} center ($S' = {}^2/_2$). The data were fitted to an isotropic spin-only exchange Hamiltonian (eq 2), S = 2/2 with a single J value ($J = J_1 = J_2$) using normal vector coupling procedures within *MAGMUN4.1*.[29] A very good fit gave $g_{ave} = 2.178(6)$, $J_1 = J_2 = -5.3(1)$ cm^{-1}, TIP = 1750×10^{-6} cm^3 mol^{-1}, $\rho = 0.0001$, and $10^2R = 1.3$. The solid lines in Figure 16 were calculated with these parameters. This exchange integral is slightly higher than values obtained for comparable Mn^{II}_9 grids but typical for comparable μ-O-bridged [2 × 2] Ni^{II} systems.[18]

Mixed-Valent Homometallic Grids. Mn^{II}, Fe^{II}, and Co^{II} ions have a propensity to undergo oxidation to higher oxidation state species, in many cases just in the presence of air. This will, in part, be dependent on the crystal-field strength at a particular coordination site, where stronger ligand-field environments would tend to favor the oxidation. The complex $[Co(II)_2Co(III)_2(poap\text{-}H)_2(poap\text{-}2H)_2](NO_3)_4 \cdot 7H_2O$ (**10**) consists of a rectangular array with four metals bridged by four ligands with two ligands in the μ-O mode and two in the μ-NN mode (Figure 17) and results from exposure of the reaction solution to air.[25] The Co^{III} sites [Co(1)] are nitrogen-rich and have N_5O coordination spheres, whereas the Co^{II} [Co(2)] sites have N_3O_3 environments. The magnetic moment varies slightly from 7.6 μ_B at 300 K to 6.6 μ_B at 4.5 K. The long distances separating the Co^{II} sites

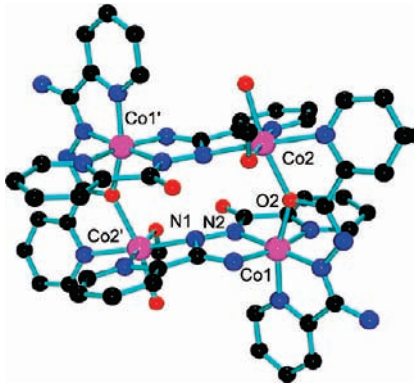

Figure 17. POVRAY structural representation of the cation in **10**.

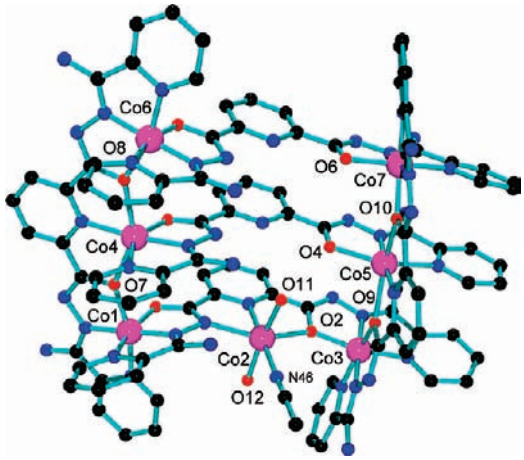

Figure 18. POVRAY structural representation of the cation in **11**.

suggest that exchange coupling would be insignificant, so that the small drop in the moment with temperature can be associated just with single-ion Co^{II} properties.[18] The reaction of 2poap with $Co(ClO_4)_2$ in air produces an unusual heptanuclear incomplete grid $[Co(III)_4Co(II)_3(2poap)_5](ClO_4)_6 \cdot 11H_2O$(**11**) (Figure 18 shows the cationic fragment), which has Co^{III} sites at the corners and Co^{II} sites at the sides of what is best described as a rectangular rather than a square structure. The Co^{III} sites have N_4O_2 coordination spheres, while the Co^{II} sites have N_3O_3 environments. The remote arrangement of the three Co^{II} centers would not be expected to lead to spin exchange, which is confirmed by variable-temperature magnetic data, with a slight drop in the magnetic moment from 9.3 μ_B at 300 K to 8.1 μ_B at 2 K. Once again single-ion Co^{II} properties reveal a quite small drop in the magnetic moment with temperature,[25] and Co^{III} appears to choose the nitrogen-rich, stronger ligand-field sites. In the related Co^{III}/Co^{II} dinuclear complex $[(ioap)_2Co_2(H_2O)_4](BF_4)_2$, the Co^{III} center occupies an N_6 coordination site in keeping with the clear preference of a strong ligand environment (vide supra) and also exhibits a small drop in the magnetic moment in the range 300−2 K.[23]

While Mn^{II} complexes of hydrazone ligands of this type appear not to be sensitive to air, Mn^{II}_9 [3 × 3] grids can be selectively oxidized either electrochemically or chemically. Controlled oxidation with Cl_2 and using electrochemical potentials <1 V (Ag/AgCl) lead to the selective oxidation of the corner Mn^{II} sites in $[Mn^{II}_9(2poap)_6](ClO_4)_6$ to Mn^{III}

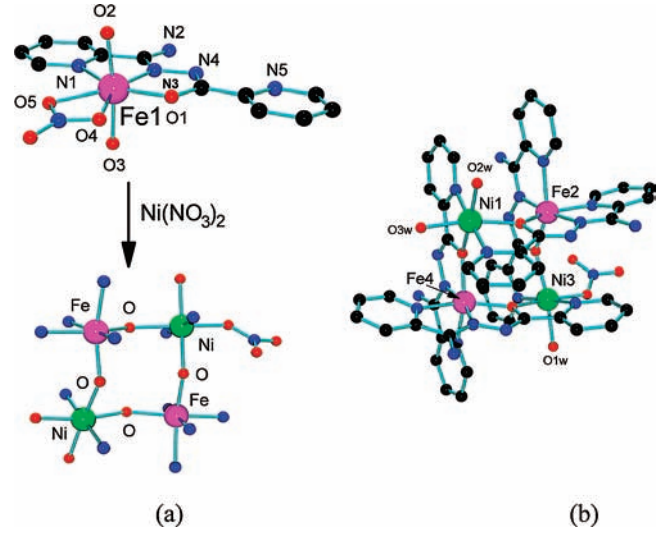

Figure 19. (a) Reaction scheme for the synthesis of **12**. (b) POVRAY structural representation of the cation in **12**.

in $[Mn^{III}_4Mn^{II}_5(2poap)_6](ClO_4)_{10}$.[27,28,31] This system is interesting magnetically as a novel example of an antiferromagnetic homometallic, heterovalent grid and exhibits a simple noncompensated $S' = {}^1/_2$ ground state as a result of the combination of $S = {}^4/_2$ (corner) and ${}^5/_2$ (center and side) spin centers. Once again the higher oxidation state sites occur in the grid pockets, which create the larger crystal fields. In the related complex $[Fe^{III}_5(Cl2poap)_6](ClO_4)_9$, which has an incomplete grid structure with metalation only at sites 1, 3, 5, 7, and 9 (Figure 10) but otherwise a complete grid arrangement of ligands, ferrimagnetic behavior would be expected but is effectively not observed directly because the coupling between the remote $S = {}^5/_2$ centers is very weak.[26] The magnetic moment drops from 13.2 μ_B at 300 K to 10.3 μ_B at 2 K ($J = -0.2$ cm^{-1}).

Heterometallic Grids. [2 × 2] Grids. Ferrimagnetic behavior can also be generated by incorporating different metal ions into an antiferromagnetic complex, with resulting noncompensation of spins. In the [2 × 2] case, this has been achieved in the square green crystalline grid complex $[Fe_2Ni_2(poap\text{-}H)_4(NO_3)(H_2O)_3](NO_3)_5 \cdot 2.5H_2O \cdot 1.75CH_3OH$ (**12**), which was produced by the reaction of the mononuclear Fe^{III} complex $[Fe(Hpoap\text{-}H)(NO_3)(H_2O)_2](NO_3)_2 \cdot 2H_2O$ (**13**)[32] with $Ni(NO_3)_2 \cdot 6H_2O$ in $MeOH/CH_2Cl_2$ (Figure 19a,b).[33] The heterometallic grid assembly follows a logical path of construction via a "complex as ligand" approach using the open coordination site in **13**, despite requiring the effective release of free ligand to complete the process. The alternating symmetrical arrangement of d^5 and d^2 centers in a typical μ-O-bridged grid leads to antiferromagnetic exchange, and as a result of the noncompensation of spins, a ferrimagnetic system with a $S' = {}^6/_2$ ground state is produced. Successful

(31) Thompson, L. K.; Kelly, T. L.; Dawe, L. N.; Grove, H.; Lemaire, M. T.; Howard, J. A. K.; Spencer, E. C.; Matthews, C. J.; Onions, S. T.; Coles, S. J.; Horton, P. N.; Hursthouse, M. B.; Light, M. E. *Inorg. Chem.* **2004**, *43*, 7605–7616.
(32) Xu, Z.; Thompson, L. K.; Matthews, C. J.; Miller, D. O.; Goeta, A. E.; Howard, J. A. K. *Inorg. Chem.* **2001**, *40*, 2446–2449.
(33) Parsons, S. R.; Thompson, L. K.; Dey, S. K.; Wilson, C.; Howard, J. A. K. *Inorg. Chem.* **2006**, *45*, 8832–8834.

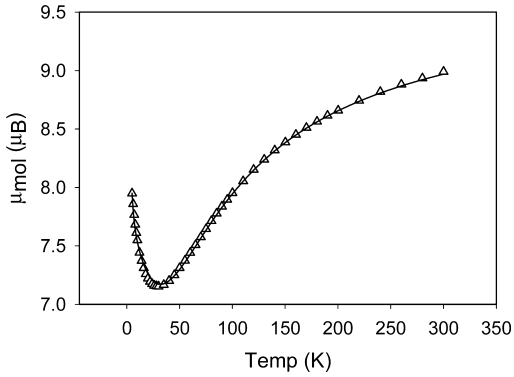

Figure 20. Variable-temperature magnetic properties of **12** (see the text for fitted parameters).

fitting of the variable-temperature magnetic data to eq 1 ($S_1 = S_3 = {}^5/_2$; $S_2 = S_4 = {}^2/_2$; Figure 20) gave $J = -15.6(5)$ cm^{-1}.[33]

[3 × 3] Grids. The systematic construction of heterometallic [3 × 3] grids is difficult using the "complex as ligand" approach described for **12** (vide supra). However, the symmetric or pseudosymmetric nature of the grid arrangement of the six ligands and nine metals in the μ-O-bridged structure arranges equivalent coordination groupings at all of the side and all of the corner positions. The fact that in the case of Mn^{II}_9 grids, e.g., **6** and $[Mn^{II}_9(2poap)_6](ClO_4)_6$ (vide supra), the corner sites are the most labile in terms of metal site oxidation suggests that metal substitution lability may also be site specific and may depend on the nature of the substituting metal ion and the particular coordination sphere. This would also make sense because the corner sites only have two μ-O bridging connections as opposed to three and four for the side and center sites, respectively. This is supported strongly also by the observation that for the Mn^{II}_9 [3 × 3] grids studied the corner sites are electrochemically oxidized first (∼0.6 V vs Ag/AgCl), in a one-step quasi-reversible process, followed by four side sites in reversible single-electron steps at increasing potentials in the range ∼1−1.5 v (vs Ag/AgCl).[27,28,31] Therefore, the synthesis of symmetric heterometallic complexes may be possible by starting with, e.g., a Mn^{II}_9 [3 × 3] grid and reacting it with a different metal ion directly. Also, the differing coordinating nature of the metal ions might allow a site preferential occupancy in a reaction in which the ligand competes with two different metal ions in a reaction mixture.

The reaction of 2pmoap with a mixture of $Mn(NO_3)_2 \cdot 6H_2O$ and $Zn(CH_3COO)_2 \cdot 2H_2O$ in methanol/acetonitrile led to the formation of **14** as orange crystals (see the Experimental Section). A structural study (Figure 21) revealed that the Zn^{II} ions occur at the side sites, while the Mn^{II} ions occur elsewhere. Abbreviated crystal data are given in Table 1, and important bond distances and angles are listed in Table 5. The structure has tetragonal crystallographic symmetry, which is manifested as effective 4-fold symmetry within the grid cation (point symmetry S_4). Metal assignment was supported by a comparison of the bond distances to previously reported [3 × 3] Zn^{II}_9 and Mn^{II}_9 grids[20,26] and upon a sensible magnetic analysis (vide infra), all of which agree with the presence of Mn^{II} ions at the center and corner sites

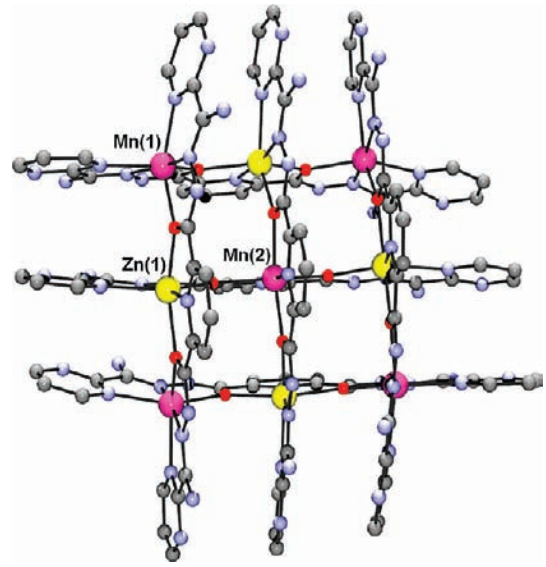

Figure 21. POVRAY structural representation of the cation in **14**.

Table 5. Bond Distances (Å) and Angles (deg) for **14**

Zn1−N15	2.071(6)	Mn1−O1	2.149(5)
Zn1−N6	2.106(6)	Mn1−N1	2.235(8)
Zn1−O3	2.116(5)	Mn1−N11	2.315(9)
Zn1−O1	2.183(5)	Mn2−N17	2.167(8)
Zn1−O2	2.212(6)	Mn2−N17	2.167(8)
Zn1−N12	2.345(7)	Mn2−O3	2.194(5)
Mn1−N4	2.004(8)	Mn2−O3	2.194(5)
Mn1−N8	2.016(7)	Mn2−O3	2.194(5)
Mn1−O2	2.116(5)	Mn2−O3	2.194(5)
Mn1−O1−Zn1	134.0(3)	Zn1−O3−Mn2	131.1(2)
Mn1−O2′−Zn1′	132.4(3)		

Table 6. Bond Distances (Å) and Angles (deg) for **16**

Cu1−N14	1.933(5)	Mn1−O1	2.228(3)
Cu1−N10	1.970(5)	Mn1−O1	2.228(3)
Cu1−O3	2.133(3)	Mn1−O1	2.228(3)
Cu1−N17	2.168(4)	Mn2−N4	2.096(4)
Cu1−O2	2.239(3)	Mn2−O1	2.153(3)
Cu1−N7	2.244(5)	Mn2−N12	2.154(4)
Mn1−N6	2.195(4)	Mn2−O2	2.192(3)
Mn1−N6	2.195(4)	Mn2−O3	2.212(3)
Mn1−O1	2.228(3)	Mn2−N1	2.328(4)
Mn2−O1−Mn1	130.11(13)	Cu1−O3−Mn2	134.11(16)
Mn2′−O2′−Cu1	134.39(15)		

and Zn^{II} at the side sites. Neither Mn^{II} nor Zn^{II} benefits from CFSE effects, and so on this basis, there is no apparent site preference. However, the preference may simply be the result of a better size match for the larger Zn^{II} ion (ionic radii: Mn^{II}, 0.67 Å; Zn^{II}, 0.74 Å). The Zn(1)−L average distance is 2.172 Å, while for Mn(1), it is 2.139 Å. The choice of Mn^{II} at the center site may be a consequence of the harder donor environment. Zn−Mn distances fall in the range 3.92−3.99 Å, with Zn−O−Mn angles in the range 131.1−134.0°.

The reaction of the complete $[Mn_9(2pmoap\text{-}2H)_6](NO_3)_6 \cdot 13H_2O$ (**15**)[20] with $Cu(NO_3)_2 \cdot 6H_2O$ in methanol/acetonitrile in the presence of triethylamine, with gentle heating for a short time, gave brown crystals (see the Experimental Section) of **16** suitable for structural analysis. Abbreviated crystallographic data are given in Table 1, and important bond distances and angles are listed in Table 6. The structure of the grid cation is shown in Figure 22 and the core structure in Figure 23. In this

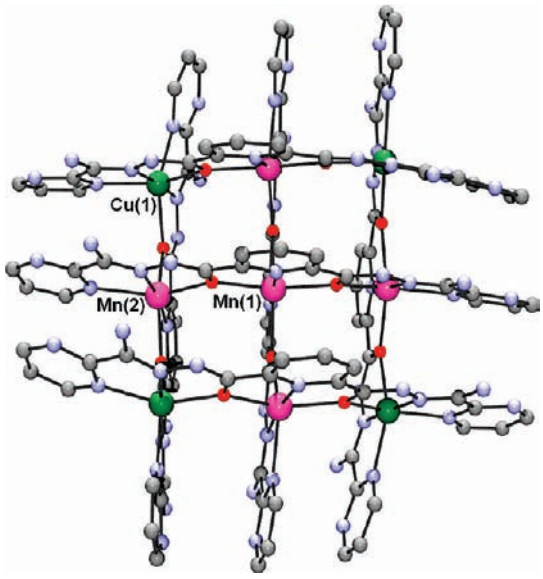

Figure 22. POVRAY structural representation of the cation in **16**.

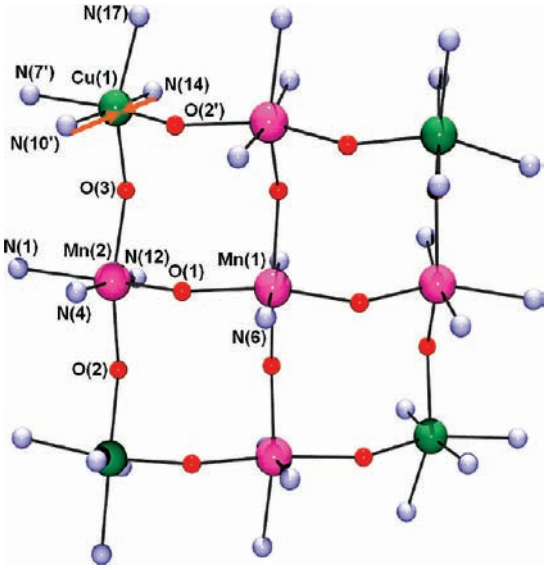

Figure 23. POVRAY structural representation of the core in **16**.

case, just the corner manganese sites are substituted by Cu^{II}. **16** exhibits tetragonal crystallographic symmetry and 4-fold symmetry within the grid cation (Figure 23), with *cis*-CuN_4O_2 coordination environments at the corner centers, *mer*-MnN_3O_3 environments at the side centers, and a *trans*-MnN_2O_4 coordination environment at the central Mn^{II} ion. Metal assignment was supported by a comparison of the bond lengths with those of the parent Mn^{II}_9 compound and to $[Cu_9(2pmoap\text{-}2H)_2(2pmoap\text{-}H)_4](ClO_4)_{10}\cdot 13.2H_2O$ (**17**), a Cu^{II}_9 [3 × 3] grid with the same ligand.[20]

Metal−metal distances fall in the range 3.972−4.084 Å, with M−O−M angles in the range 130.1−134.4°. The side manganese centers display long Mn−N distances to the external pyrimidine rings [2.327(4) Å], with shorter remaining Mn−N contacts [2.096(4) and 2.155(4) Å] similar to those reported for **15** [2.373(5) and 2.145−2.183 Å, respectively], while the central manganese ion has Mn−N and Mn−O bond distances of 2.198(5) and 2.226(3) Å, respectively, also comparable to those in **15** [2.182(5) and 2.199(3) Å, respectively]. Cu(1) has an axially compressed geometry, resulting in a d_{z^2} magnetic ground state (arrows in Figure 23), with long contacts to N(7′), N(17), O(2′), and O(3) (2.134−2.244 Å) and short bonds to N(10) and N(14) [1.970(5) and 1.931(5) Å, respectively]. For comparison, the central Cu^{II} ion in **17** also exhibits axial compression with four long contacts measuring 2.203(3) Å and two short measuring 1.936(6) Å.[20]

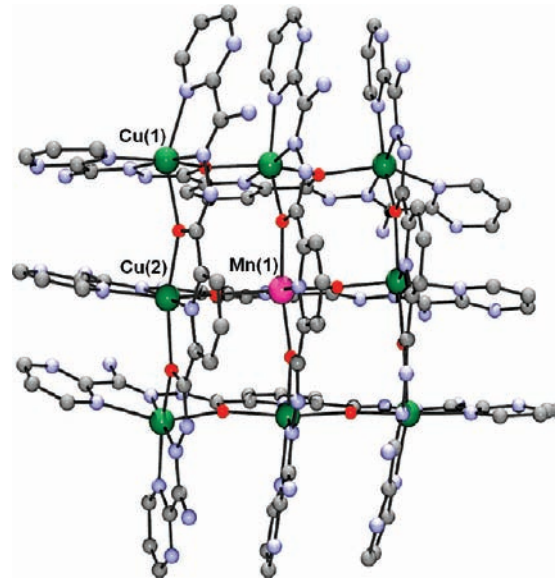

Figure 24. POVRAY structural representation of the cation in **18**.

The reaction of **15** with $Cu(NO_3)_2\cdot 6H_2O$ in methanol/acetonitrile in the absence of a base, but under more vigorous extended reflux conditions (see the Experimental Section), led to the more copper-rich heterometallic complex **18** as brown crystals. Diffraction data were collected successfully, but only to $2\theta = 46.4°$ (tetragonal, $I4_1/acd$; $a = 27.889(3)$ Å, $c = 39.039(4)$ Å; isostructural with **15** and **16**). Consequently, although a solution was obtained, only a limited report will be presented at this time (see the Supporting Information for a CIF file). The structure of the cationic fragment of **18** and its core structural representation are shown in Figures 24 and 25, respectively. Compound **18** exhibits the normal [3 × 3] grid arrangement with tetragonal crystallographic symmetry and 4-fold symmetry within the grid cation (Figure 25). Metal assignment was supported by a comparison of the bond lengths to those of the parent [3 × 3] Mn^{II}_9 grid (**15**) and to the [3 × 3] Cu^{II}_9 grid (**17**), as well as from a sensible magnetic analysis (vide infra). All agree with the presence of a Mn^{II} ion at the center pocket of **18**, with Cu^{II} at the side and corner sites.

Metal−metal distances fall in the range 4.01−4.25 Å, with M−O−M angles in the range 135.7−138.3°. Each copper ion has a Jahn−Teller distorted, axially elongated octahedral geometry (highlighted by the arrows in Figure 25). Cu(1) has a $d_{x^2-y^2}$ magnetic ground state as defined by short contacts to N(4), N(8′), N(11′), and O(2′) (average 2.035 Å) with long axial contacts to N(1) and O(1) (average 2.271 Å). Cu(2) also exhibits a $d_{x^2-y^2}$ ground state with short contacts to N(6), N(12), N(15), and O(3) (average 2.067 Å) and long axial

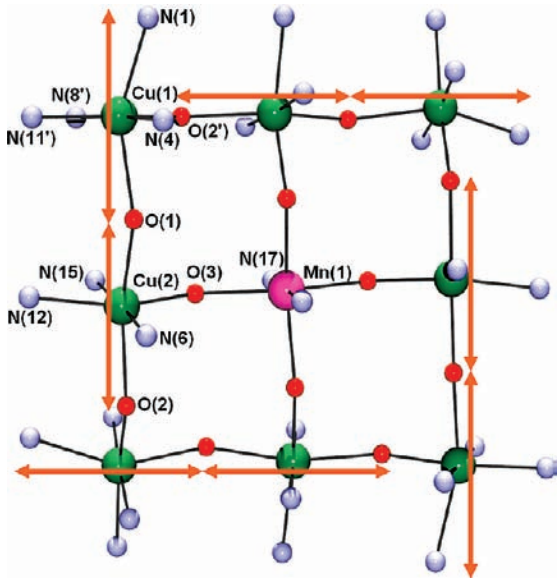

Figure 25. POVRAY structural representation of the core in **18** (arrows indicate the Jahn−Teller axes).

contacts to O(1) and O(2) (average 2.251 Å). These values are comparable to those for the Cu^{II} ions in the outer ring of **17**, which also have $d_{x^2-y^2}$ magnetic ground states (average short 2.025 Å and average axial 2.273 Å). Mn(1) exhibits bond lengths that are consistent with those observed for the central Mn ion in **15**. This arrangement sets up orbitally orthogonal magnetic connections in the outer ring of eight copper ions, with nonorthogonal connections between Mn(1) and its neighbors, leading to ferrimagnetic behavior (vide infra).

Magnetic Properties. The description of a magnetic exchange model for the [3 × 3] $Mn^{II}_5M^{II}_4$ grids (where M = Zn, Cu) depends on the position of the heteroatom within the grid. For **14** with diamagnetic Zn^{II} ions at the side positions, exchange coupling between the remote Mn^{II} sites would be considered to be quite weak or nonexistent (Figure 10; 2, 4, 6, and 8 = Zn^{II}). The magnetic moment for **14** drops slightly from 13.3 μ_B at 300 K to 12.9 μ_B at 40 K, consistent with the presence of five remote Mn^{II} ions, followed by a more pronounced decrease to 10.1 μ_B at 2 K (Figure 26). This decrease could be attributed to zero-field splitting effects. However, these are normally quite small for Mn^{II}, and it is reasonable to assume that it is due instead to weak, long-range antiferromagnetic coupling between Mn^{II} centers via the intervening Zn^{II} sites. The isotropic exchange Hamiltonian describing this Mn^{II}_5 exchange situation is expressed in eq 6 (see Figure 10 for site numbering; one J value is considered reasonable given the effective equivalence of all bridging connections).

$$H_{ex} = -J(S_1 \cdot S_7 + S_1 \cdot S_9 + S_1 \cdot S_3 + S_5 \cdot S_7 + S_5 \cdot S_9 + S_5 \cdot S_3) \quad (6)$$

The experimental magnetic data were fitted by nonlinear regression within *MAGMUN4.1*[29] to give $g = 2.00(6)$, $J = -0.148(8)$ cm^{-1}, TIP = 20×10^{-6} cm^3 mol^{-1}, $\rho = 0.10$, and $10^2R = 2.39$ ($R = [\sum(\chi_{obsd} - \chi_{calcd})^2/\sum\chi_{obsd}^2]^{1/2}$). The solid line in Figure 26 was calculated with these parameters.

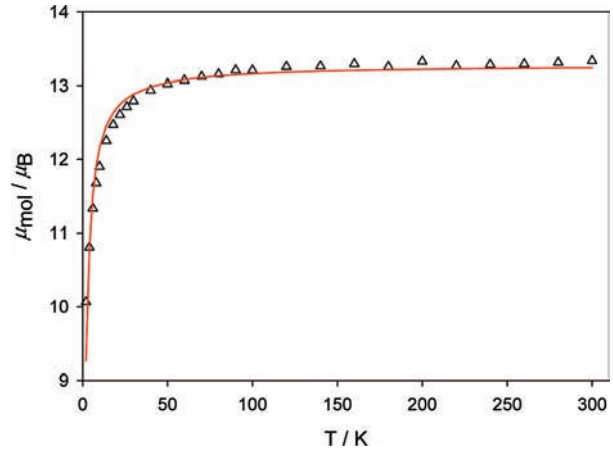

Figure 26. Variable-temperature magnetic data for **14** (see the text for fitted parameters).

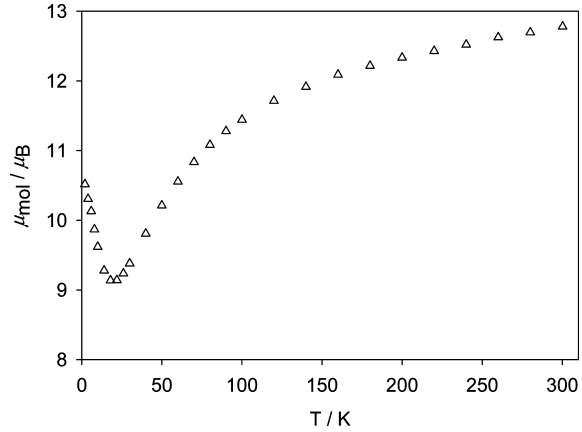

Figure 27. Variable-temperature magnetic data for **16**.

The J value is reasonable given the large separation between the Mn^{II} centers and is comparable to the result obtained for an incompletely metalated Fe^{III}_5 square grid $[Fe_5(Cl2poap)_6](ClO_4)_6 \cdot 11H_2O$, formed from the self-assembly of $Fe(ClO_3)_2 \cdot 6H_2O$ with Cl2poap (Chart 1),[26] in which the six ligands adopt the normal arrangement for a [3 × 3] grid but the Fe^{III} ions ($S = {}^5/_2$; the same spin states as Mn^{II}) occupy only the center and corner grid positions. The side metal sites are vacant. Magnetic data for this compound fitted to the same model gave $g = 2.015$, $J = -0.2$ cm^{-1}, and TIP = 200×10^{-6} cm^3 mol^{-1},[26] clearly a comparable exchange situation. In reality, this represents a potentially ferrimagnetic situation because of the arrangement of the $S = {}^5/_2$ Mn^{II} and $S = 0$ Zn^{II} centers, but larger values of $|-J|$ would be required to observe the expected rise in the magnetic moment at low temperatures due to noncompensation of spins. This would, however, be expected for a grid with more direct exchange connections.

16 has Cu^{II} ions only at the corner sites (Figure 10; 1, 3, 5, and 7 = Cu^{II}). This arrangement of different spins ($S = {}^5/_2, {}^1/_2$) in a [3 × 3] antiferromagnetic grid would be expected to lead to noncompensation of spins in the ground state and ferrimagnetic behavior. Figure 27 shows that the magnetic moment for **16** drops from 12.8 μ_B at 300 K to about 9.1 μ_B at approximately 20 K, followed by a rise at lower temperature, indicative of intramolecular antiferromagentic ex-

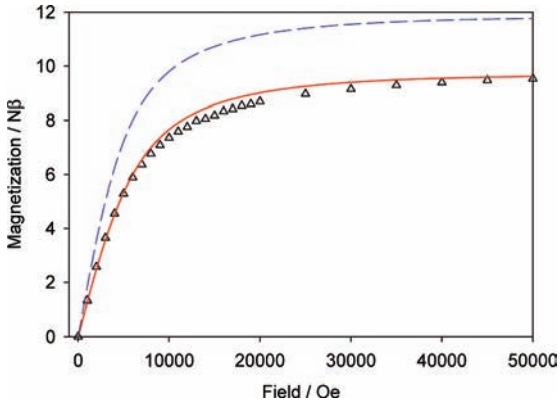

Figure 28. Variable-field magnetization data for **16**. The solid red line was calculated for $g = 2.15$, $S' = {}^{9}/_{2}$, and $T = 2$ K, and the dashed blue line was calculated for $g = 2.15$, $S' = {}^{11}/_{2}$, and $T = 2$ K, using the appropriate Brillouin function.

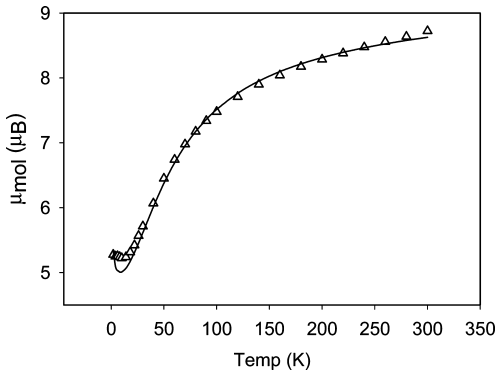

Figure 29. Variable-temperature magnetic data for **18** (see the text for fitted parameters).

change and a high-spin ground state. Theoretical calculations show that the expected ground state should be $S' = {}^{11}/_{2}$. However, the low-temperature (2 K) magnetic moment suggests a slightly smaller ground state, and magnetization data as a function of the field (Figure 28) show that the ground state is closer to ${}^{9}/_{2}$ (assuming a reasonable g value). Theoretical calculations for this spin model show that, depending on the choice of coupling constants, there is a low-lying $S' = {}^{9}/_{2}$ spin state that is energetically close to the $S' = {}^{11}/_{2}$ ground state. It is therefore possible that at the lower experimental temperature limit (2 K) the real ground state is not being populated significantly but could be populated at some temperature below 2 K. No discernible hysteresis was observed for **16** at 2 K. No attempt was made to fit the magnetic data to the appropriate exchange model, but it is clear that exchange coupling is antiferromagnetic.

The magnetic data for the [3 × 3] $Mn^{II}_{1}Cu^{II}_{8}$ grid **18** are shown in Figure 29 as a plot of the magnetic moment per mole as a function of the temperature. The magnetic moment drops from 8.7 μ_B at 300 K to a plateau value of approximately 5.2 μ_B between 18 and 2 K, suggesting a dominant antiferromagnetic exchange component. The slight rise in the magnetic moment <18 K suggests that there may also be a ferromagnetic exchange component present as well. The room temperature value is slightly higher than expected for a typical combination of eight Cu^{II} centers (e.g., $g = 2.2$) and one Mn^{II} center ($g = 2.0$) (8.2 μ_B). **18** exhibits 4-fold symmetry within the grid cation, as seen from the crystal structure, which is useful in an attempt to interpret the magnetic connectivity and the modeling of the experimental data. The corner and side sites have distorted octahedral geometries and exhibit Jahn−Teller elongation, consistent with their assignment as copper centers [Cu(1) and Cu(2); Figure 25]. This would define their magnetic ground states as $d_{x^2-y^2}$. The long axis for Cu(1) points toward O(1) with a short connection directed toward O(2′), while for Cu(2), the long axis is directed toward both O(1) and O(2) with a short connection to O(3) (Figure 25). On the basis of the directionality of the Jahn−Teller axes in the outer Cu^{II}_{8} ring, the Cu(1)−O(2′)−Cu(2′) and Cu(2)−O(1)−Cu(1) connections should be orthogonal, while the Cu(2)−O(3)−Mn(1) connection is not. These structural features would suggest ferromagnetic coupling between the Cu(1) and Cu(2) centers (and their symmetry-related counterparts) and that a single exchange constant can be used to model the ring's contribution to the observed magnetic properties (J_1; Figure 10). Unlike the Jahn−Teller-distorted Cu^{II} centers, the central Mn^{II} ion is magnetically isotropic, with electron density along all axes, leading to antiferromagnetic exchange between the Cu(2) centers and Mn(1) (J_2; Figure 10) via the nonorthogonal Cu(2)−O(3) connections.

The magnetic data for **18** were fitted to a model incorporating both ferromagnetic and antiferromagnetic terms (vide supra) within *MAGMUN*[29] to give $g_{ave} = 2.3(1)$, $J_1 = 0.45(2)$ cm^{-1}, $J_2 = -22.5(2)$ cm^{-1}, TIP = 1000×10^{-6} cm^3 mol^{-1}, $\rho = 0.055$, and $\theta = 0.5$ K ($10^2R = 2.2$) (see the solid line in Figure 29). The large "g_{ave}" value would be dominated by copper and is typical of Cu_9 ferromagnetic grids and may be associated with the highly distorted copper coordination spheres. The small positive J value for Cu−Cu coupling is also characteristic of these copper grids.[20] The J_{Mn-Cu} coupling constant cannot be compared directly with literature values because of the paucity of such systems, but in a macrocyclic Cu−Mn complex with two phenoxide bridges (Mn−O−Cu = 100.1° and 101.6°), J was found to be −36.8 cm^{-1}.[34] The paramagnetic impurity contribution would reasonably be from a small amount of a grid species with some additional Mn^{II} content, not revealed from either the structure or the elemental analysis. Metal analyses were not attempted but would not have been successful in distinguishing such components. The J_1 and J_2 values are reasonable in terms of the anticipated ferromagnetic ring contribution and the internal antiferromagnetic term. A magnetization versus field study at 2 K showed a smooth rise in M with increasing field from 0 to 4.8 Nβ at 50 000 Oe, a value somewhat higher than expected based on the nominal ground state for the Cu_8Mn model of ${}^{3}/_{2}$. This may be associated with the presence of some manganese-rich impurity.

[4 × 4] Grids. The ligand control during self-assembly demonstrated in the [2 × 2] and [3 × 3] cases indicates great thermodynamic stability of the basic grid structures comprised of metal ions bridged by μ-$O_{hydrazone}$ linkages. Pro-

(34) Bo, L.; Hong, Z.; Zhi-Quan, P.; You, S.; Cheng-Gang, W.; Han-Ping, Z.; Jing-Dong, H.; Ru-An, C. *J. Coord. Chem.* **2006**, *59*, 1271–1280.

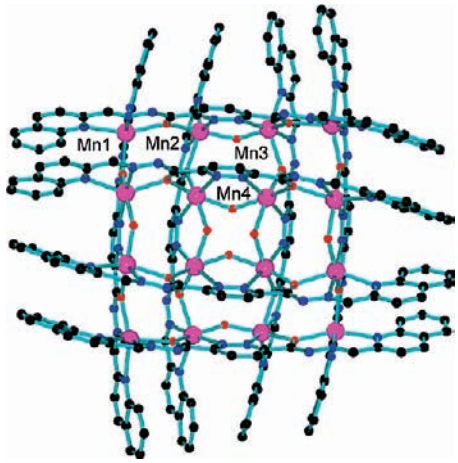

Figure 30. POVRAY structural representation of the cation in **19**.

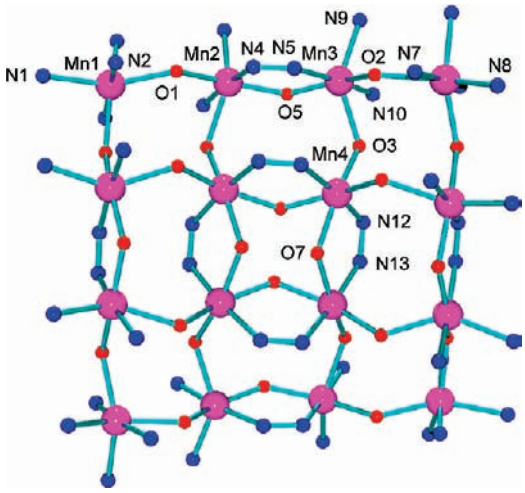

Figure 31. POVRAY structural representation of the core in **19**.

gramming this coordination element into larger symmetric ligands has been carried out, with the synthesis and study of tetratopic ligands, e.g., L2−L7 (Chart 1), based on central disubstituted pyridazine and pyrazole fragments. [4 × 4] Mn^{II}_{16} grids form readily with L3−L5. The structure of the red-orange complex $[Mn_{16}(L4)_8(OH)_8](NO_3)_8 \cdot 15H_2O$[14,16] has already been reported. A new grid **19** (see the Experimental Section) is shown in Figure 30 and consists of a grid array of 16 six-coordinate pseudooctahedral Mn^{II} ions embedded within a group of eight ligands, arranged in two roughly parallel groups of four above and below the metal pseudoplane. The core structure (Figure 31) shows that there are four groups of $[Mn_4(\mu\text{-}O)_4]$ square subunits bridged internally by $\mu\text{-}O_{hydrazone}$ groups, with each of these subunits bridged by a combination of μ-NN (pyridazine) and μ-O groups to their neighbors. Abbreviated crystal data are given in Table 1, and important distances and angles are listed in Table 7. The ligands differ from their tritopic pyridine-based counterparts in that they form heteroleptic complexes with six-coordinate metal ions, and the unsaturated Mn^{II} centers in the central pyridazine-bridged core pick up exogenous oxygen-based bridging groups, clearly scavenged from the solvent during synthesis. Mn−O distances to bridging oxygen O(5) are very short (2.064 and 2.076 Å), while those to O(7) and disordered counterpart O(6) (not shown) are very much longer (2.137 and 2.149 Å). This suggests that O(5) is oxide, while O(7) is hydroxide, in keeping with elemental analytical data. Protons for the cationic fragment of **19** were found in the difference map, and one [H(33)] bound to O(6)/O(7) confirms this site as hydroxide. No protons were present on the bridging atom O(5), supporting the identity of this bridge as oxide. Furthermore, only one full-occupancy nitrate was present in the asymmetric unit, and there was no evidence for additional nitrate anions. Mn−O−Mn bridge angles fall in the range 124.3−129.8 ° (average 127.2°) within each corner Mn_4 grouping and are 119.8° at O(6)/O(7) and 130.8° at O(5). The angles at O(5) and O(6)/O(7) are again consistent with oxide and hydroxide, respectively. Mn−Mn separations fall in the range 3.9−4.1 Å within the square corners but are much shorter via the pyridazine bridges [3.764 Å for Mn(2)−Mn(3) and 3.709 Å between symmetry-related Mn(4) centers]. The connected μ-O and μ-NN bridging arrangement suggests that the exchange coupling between metals will be antiferromagnetic.

Table 7. Bond Distances (Å) and Angles (deg) for **19**

Mn1−N7	2.150(7)	Mn3−N10	2.185(6)
Mn1−N2	2.176(6)	Mn3−O2	2.214(5)
Mn1−O1	2.250(5)	Mn3−O3	2.263(5)
Mn1−O2	2.282(5)	Mn3−N5	2.272(6)
Mn1−N8	2.286(6)	Mn3−N9	2.335(6)
Mn1−N1	2.373(6)	Mn4−O7	2.138(10)
Mn2−O5	2.064(5)	Mn4−O6	2.144(9)
Mn2−N15	2.183(6)	Mn4−O7	2.149(10)
Mn2−O1	2.215(5)	Mn4−O6	2.153(9)
Mn2−N4	2.267(6)	Mn4−O4	2.194(5)
Mn2−O4	2.302(5)	Mn4−O3	2.195(5)
Mn2−N16	2.344(6)	Mn4−N12	2.286(6)
Mn3−O5	2.077(5)	Mn4−N13	2.306(6)
Mn2−O1−Mn1	128.7(2)	Mn2−O5−Mn3	130.8(3)
Mn3−O2−Mn1	129.8(2)	Mn4−O6−Mn4	119.4(5)
Mn4−O3−Mn3	124.3(2)	Mn4−O7−Mn4	119.8(5)
Mn4−O4−Mn2	126.1(2)		

Variable-temperature magnetic data for **19** show a steady drop in the magnetic moment from ∼22 μ_B to ∼4 μ_B at 2 K (Figure 32), a clear indication of intramolecular antiferromagnetic exchange. The enormity of the calculations of the spin states for such a system has precluded any detailed analysis of the exchange problem. However, because the grid can be considered as a composite of four [2 × 2] Mn_4 $\mu\text{-}O_{hydrazone}$-bridged subunits, a simplified approach was taken based on the square corners.

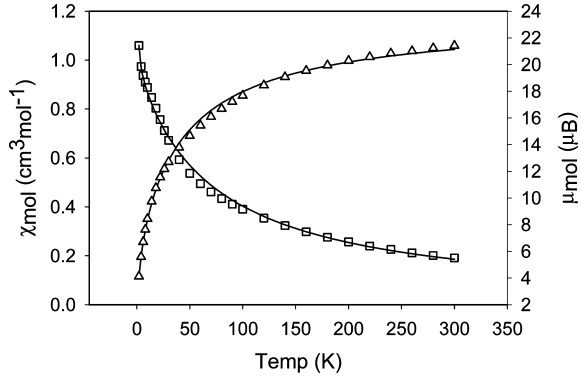

Figure 32. Variable-temperature magnetic data for **19** (see the text for fitted parameters).

$$H_{ex} = -J\{S_1 \cdot S_2 + S_2 \cdot S_{13} + S_{13} \cdot S_{12} + S_{12} \cdot S_1\} \quad (7)$$

$$X_{mol} = g^2 N\beta^2 f(J,T)/[kT - zJ' f(J,T)] \quad (8)$$

The magnetic model is shown in Figure 33 and treats the Mn_4 squares independently (eq 7), with a molecular field correction term (eq 8) to approximate the interaction between the Mn_4 subunits and scaling of the magnetic data per mole. An excellent fit was obtained to eq 8 with $g = 2.0$, $J = -0.35$ cm^{-1}, $J' = -4.25$ cm^{-1}, $\rho = 0.019$, and $z = 2$ ($10^2R = 2.3$). Molecular-field correction terms are normally small exchange perturbations based on "long-range" weak interactions between coupled subunits. However, in the present case, the fitted J' value is large by these standards but in line with the close proximity of the connected square corner subunits and the multiple bridging arrangement. The solid line in Figure[32] was calculated with these parameters. The intrasquare (Mn_4) J value is smaller than that observed for isolated [2 × 2] Mn_4 squares (e.g., **1**),[20] but considering the bridging connectivity between the square subunits, this is not unreasonable. The double pyridazine/oxide−hydroxide combinations, particularly oxide with large Mn−O−Mn angles (130.8°) and short Mn−O distances, would clearly dominate the exchange coupling, and so despite the simplicity of the model, it is eminently sensible.

Cu^{II} forms similar [4 × 4] grids with tetratopic pyridazine ligands with the same architecture. The complex $[Cu_{16}(L5)_8(O)_2(OH)_4(H_2O)_2](CF_3SO_3)_6 \cdot 66H_2O \cdot 10CH_3OH$ (**20**) involves 16 six-coordinate Cu^{II} ions arranged in the same structural pattern as **19** but with a mixture of oxide, hydroxide, and water bridges acting in combination with the pyridazine bridges.[15] The copper ions are Jahn−Teller-distorted, and the orientations of the Jahn−Teller axes lead to some bridging connections within the grid being orthogonal magnetically. The appropriate exchange model is shown in Figure 34, with J_1 and J_2 indicating the nonorthogonal connections that contribute to magnetic orbital overlap via the bridging atoms and lead to antiferromagnetic contributions. The overall symmetry of the grid allows a simplification of the coupling situation and reduces the Hamiltonian to a two J (J_1 and J_2) exchange problems (eq 9).

$$H_{ex} = -J_1\{S_2 \cdot S_3 + S_8 \cdot S_9\} - J_2\{S_5 \cdot S_6 + S_{11} \cdot S_{12}\} - [J_1\{S_{13} \cdot S_{16} + S_{14} \cdot S_{15}\} + J_2\{S_{13} \cdot S_{14} + S_{15} \cdot S_{16}\}] \quad (9)$$

The magnetic properties of this Cu_{16} grid are dominated by antiferromagnetic exchange, with fitted J values of $J_1 = -45$ cm^{-1} and $J_2 = -350$ cm^{-1} ($g = 2.21$ and TIP = 800 × 10^{-6} cm^3 mol^{-1}), where J_1 is reasonably associated with just a pyridazine bridge and J_2 with a combination of pyridazine and a large Cu−O−Cu angle oxygen atom bridge between copper centers.[15]

We now report an unusual new Cu_{16} square grid, in which the selective reduction of four sites has occurred, giving a $Cu^{II}_{12}Cu(1)_4$ mixed-valence [4 × 4] grid. The reaction of $Cu(CF_3SO_3)_2 \cdot xH_2O$ with L5 in the presence of $KAg(CN)_2$ led to the formation of the dark red-brown crystalline product **21** (see the Experimental Section). The hexadecanuclear structure of **21** is shown in Figure 35, with a core structure shown in Figure 36. Abbreviated crystal data are given in Table 1, and important bond distances and angles are listed in Table 8. The structure is similar to those of **19** and **20**, in the sense that eight ligands encompass the 16 metal ions in a 4 × [2 × 2] grid arrangement, but in this case, there are no adventitious solvent-based (O) bridging groups within the segments of the grid where copper centers are bridged by the pyridazine groups. This may have resulted because no base was added in the synthesis of **21**. Also copper can exist comfortably with coordination numbers of five and even four in the 2+ state, and so extra ligands are not essential, as they would be for a six-coordinate metal ion. In this context, the central group of four copper ions [Cu(1)N_2O_2] are four-coordinate, with unusual distorted tetrahedral geometries [L−Cu(1)−L angles 71.3−145.7°]. The corner Cu(3) sites are distorted six-coordinate (CuN_4O_2), typical of other Cu^{II}

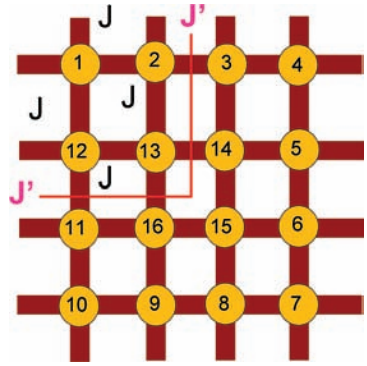

Figure 33. Magnetic exchange model for **19**.

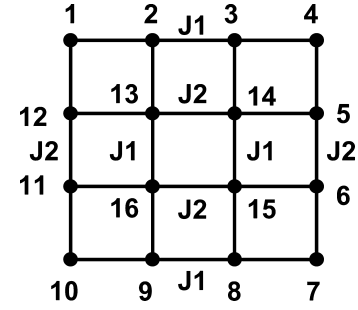

Figure 34. Magnetic exchange model for **20**.

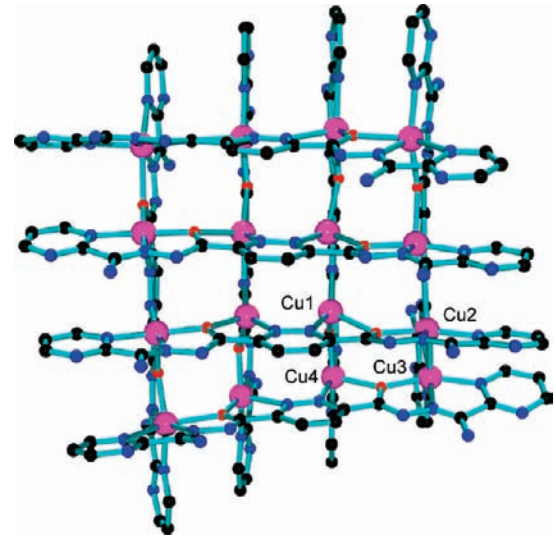

Figure 35. POVRAY structural representation of the cation in **21**.

Table 8. Bond Distances (Å) and Angles (deg) for **21**

Cu1−N18	2.107(8)	Cu3−N9	1.978(7)
Cu1−N19	2.161(7)	Cu3−O1	2.021(5)
Cu1−O4	2.286(5)	Cu3−N1	2.061(6)
Cu1−O3	2.348(5)	Cu3−O2	2.340(5)
Cu2−N16	1.890(7)	Cu3−N12	2.386(7)
Cu2−O2	1.941(5)	Cu4−N21	1.903(7)
Cu2−O3	1.982(6)	Cu4−O4	1.952(6)
Cu2−N13	2.047(7)	Cu4−N6	2.013(6)
Cu2−N7	2.296(6)	Cu4−N24	2.014(7)
Cu3−N4	1.918(7)	Cu4−O1	2.213(6)
Cu3−O1−Cu4	140.1(3)	Cu2−O3−Cu1	134.4(3)
Cu2−O2−Cu3	131.1(3)	Cu4−O4−Cu1	134.7(3)

grids in this class, while the side sites [Cu(2) and Cu(4)] are square-pyramidal (CuN_3O_2). BVS calculations have some value in assigning oxidation states but are subject to variations based on the special coordination environments created in such grids, where unusual bond lengths occur because of electrostatic repulsion, and other effects, which are brought to bear as the ligands assume their grid positions. BVS values for Cu(2), Cu(3), and Cu(4) (1.37, 1.43, and 1.43 respectively) are assigned to Cu^{II}, while the value for Cu(1) (0.64) clearly cannot be associated with Cu^{II} and is therefore assigned to Cu^{I}.[30] This would be entirely consistent with the very unusual distorted tetrahedral geometry at Cu1, which would not normally be typical for Cu^{II}. Comparable values for corner, side, and center six-coordinate sites in a Cu^{II}_9 grid involving the ligand 2pmoap are 1.40, 1.38, and 1.30, respectively.[20] Also the clear presence of 12 $CF_3SO_3^-$ anions in the structure of **21** creates a sensible charge balance for the presence of four Cu^{I} ions, on the normal assumption that each ligand loses two protons upon grid formation.

The unusual redox reaction leading to the formation of **21** appears likely to be based on the presence of $Ag(CN)_2^-$ and on the fact that CH_3CN was used in the synthetic solvent mixture, which helps to stabilize Cu^{I}. However, in the present case, it seems likely that cyanide is also involved, which may have resulted from hydrolysis of $Ag(CN)_2^-$. Subsequent catalytic oxidation of CN^- to, e.g., cyanate by air could conceivably lead to Cu^{II} reduction, thus providing a source of Cu^{I}.[35]

Cu−Cu separations within the symmetry-related Cu_4 square corner subunits fall in the range 3.900−3.996 Å, while

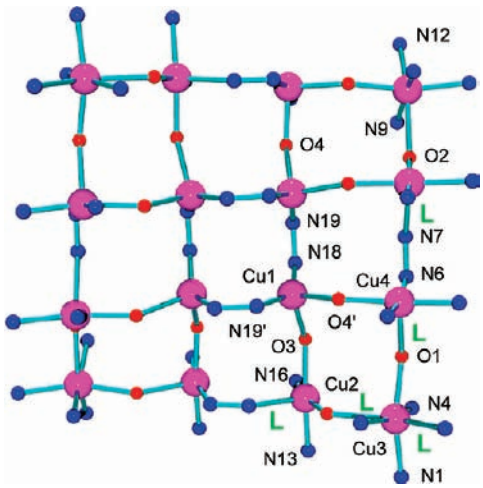

Figure 36. POVRAY structural representation of the core in **21**.

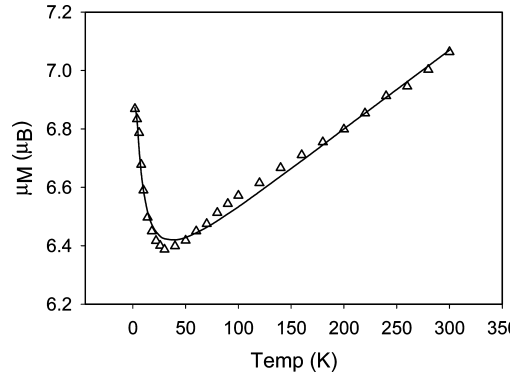

Figure 37. Variable-temperature magnetic data for **21** (see the text for fitted parameters).

the central Cu(1) ions are separated by 3.317 Å. Cu−O−Cu angles fall in the range 131.8−140.2°. The Cu(2), Cu(3), and Cu(4) sites are Jahn−Teller-distorted ($d_{x^2-y^2}$ ground states), and the elongated bonds (L) are highlighted in Figure 36. The consequences of the resulting connectivity to the neighboring copper sites have important implications for the magnetic properties (vide infra) and show that all of the connections between these sites are orbitally strictly orthogonal. This would predictably lead to ferromagnetic spin exchange (vide infra).

Variable-temperature magnetic data for **21** are shown in Figure 37 as a plot of the magnetic moment (per mole) as a function of the temperature. The magnetic moment drops from 7.1 μ_B at 300 K to 6.4 μ_B at 30 K, followed by a rise to 6.9 μ_B at 2 K. The overall magnetic moment variation is quite small (~0.7 μ_B). The low-temperature rise in the magnetic moment suggests that ferromagnetic exchange contributes to the magnetic properties as a whole, while the drop from 300 to 30 K might suggest that antiferromagnetic exchange also was a factor. However, because the inner-square metal arrangement consists of four diamagnetic Cu^{I} ions, it is reasonable to assume that there will be no significant exchange across this subunit between the distant, connected Cu^{II} ions. Therefore, the magnetic connections in **21** are defined by the orbital orientations of the 12 Cu^{II} ions in the outer-square Cu_{12} framework of the grid, and as shown in Figure 36, all of these connections are orthogonal. The three Cu^{II} ions in each square corner subunit are bridged by hydrazone oxygen atoms with large bridge angles. On the basis of previously studied Cu_4 and Cu_9 orthogonally bridged square grids, ferromagnetic exchange would be anticipated despite this large angle. However, the longer, orthogonal, three-bond pyridizine bridges (N6−N7) would perhaps not be considered significant by comparison, and so the corner groupings of three copper ions would likely dominate the exchange process.

A simple magnetic model for the grid would therefore be an alternating chain of Cu^{II} centers representing the outer-square Cu^{II}_{12} framework. However, given the long orthogonal pyridazine connections, a simpler trinuclear model seems more appropriate (vide supra). The data for **21** were

(35) For example, see: (a) Beattie, J. K.; Polyblank, G. A. *Aust. J. Chem.* **1995**, *48*, 861–868.

consequently fitted to a linear trinuclear model with a single J value ($H_{ex} = -J\{S_1 \cdot S_2 + S_2 \cdot S_3\}$) to describe just the corner subunits in essential isolation. The solid line in Figure 37 shows the best fit of the data to this model for $g_{ave} = 2.064$, $J = 4.5$ cm^{-1}, $\theta = -0.4$ K, $\rho = 0.003$, and TIP $= 1200 \times 10^{-6}$ cm^3 mol^{-1} ($10^2R = 0.57$; $R = [\sum(\chi_{obsd} - \chi_{calcd})^2/\sum\chi_{obsd}^2]^{1/2}$; θ is a Weiss correction, ρ is the fraction of paramagnetic impurity, and TIP is temperature-independent paramagnetism). The positive J value is consistent with the orthogonal nature of the bridging arrangement and with other related systems.[20] Of particular interest is the fact that in such a large metallic assembly TIP will clearly make a very significant contribution and in this case can account directly for the downward trend in the magnetic moment from 300 to 30 K. There is, therefore, no requirement for any antiferromagnetic exchange term, in agreement with the structure.

The potentially tetratopic pyrazole-based ligands L6 and L7 (Chart 1) have also been studied but so far have only produced dinuclear derivatives with copper, e.g., $[(L6)Cu_2(OH)(NO_3)(H_2O)](NO_3)\cdot 2H_2O$.[16] Although the two copper ions are bridged by the pyrazole group (and an adventitious hydroxide), the ligand adopts a ketonic syn conformation, in which the ketone groups are external to the dinuclear Cu^{II} center.

This conformation will prevent normal μ-O-bridged grid formation, and this may be associated with the rather pronounced bend in the putative hydrazone-bridged arrangement (Chart 1), compared with the analogous pyridazine ligands and considered necessary for [4 × 4] grid formation.

[5 × 5] Grids. The quest for larger magnetic $[n \times n]$ grids rests in large measure with the synthetic challenges of producing suitable polytopic ligands. L8 is a pentatopic ligand, built on construction principles similar to those of the tritopic and tetratopic ligands, by symmetric extension via hydrazone precursors. The central hydrazone is extended by reaction with an acyl ester (e.g., methylbenzoyl formate) to create an extended diester, which is then extended to the bis-hydrazone and terminated with the imidate end group.[16] The synthesis of self-assembled $[n \times n]$ (e.g., $n = 5$) grids of this size is constrained by the normal ligand substitution issues (vide supra) because the ligand donors compete for coordination sites on solvated metal cation precursors but also by the organizational problems of aligning 10 ligands and 25 metal ions in an appropriate grid arrangement.

$$6LH_2 + 9[M^{II}(L')_6]^{2+} \rightarrow [M^{II}{}_9(L^{2-})_6]^{6+} + 12H^+ + 54L' \quad (\Delta n = 52) \quad (10)$$

$$8LH_2 + 16[M^{II}(L')_6]^{2+} \rightarrow [M^{II}{}_{16}(L^{2-})_8]^{6+} + 16H^+ + 96L' \quad (\Delta n = 89) \quad (11)$$

$$10LH_2 + 25[M^{II}(L')_6]^{2+} \rightarrow [M^{II}{}_{25}(L^{2-})_{10}]^{6+} + 20H^+ + 150L' \quad (\Delta n = 136) \quad (12)$$

Entropic considerations are clearly important as part of the thermodynamic balance associated with the formation of intermediate species and fully assembled grids. Equations 10−12 highlight the entropy effect associated with the displacement of very large numbers of solvent molecules from the metal ion coordination spheres because ligand substitution takes place for [3 × 3], [4 × 4], and [5 × 5] grids. The number of (idealized) independent particles released as a function of the grid size goes up as the grid size itself increases. Therefore, there is clearly a thermodynamic advantage to the assembly of the $[n \times n]$ grids, and because they form in reasonable yields, the stability of the grids themselves must also be an important factor.

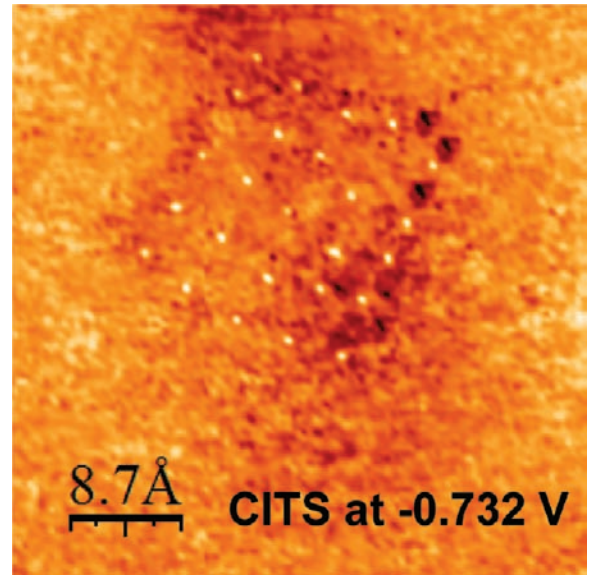

Figure 38. CITS imagery for [5 × 5] Mn_{25} grid **22**.

Crystalline samples of Mn^{II} complexes of L8 have been obtained, but thus far a structural characterization has not been achieved because of poor crystal quality and poor X-ray diffraction. The complex $[Mn_{25}(L8)_{10}](ClO_4)_{20}\cdot 65H_2O$ (**22**) has been characterized, and in an unprecedented structural approach current-imaging tunneling spectroscopy (CITS) imagery on a graphite (HOPG) surface was used to locate the grid-based positions of the 25 metal ions with separations and overall dimensions entirely consistent with a [5 × 5] grid arrangement.[16] Figure 38 shows the metal ion positions with spacing in agreement with what would be expected based on a grid array of 10 ligands encompassing the 25 metals in a μ-O-bridged arrangement analogous to the [3 × 3] Mn_9 grids.

Antiferromagnetic exchange would be expected, based on this projected structural motif. Variable-temperature magnetic data show a room temperature magnetic moment for **22** of 29.1 μ_B, consistent with 25 Mn^{II} centers (5.8 μ_B per metal) in an antiferromagnetic grid. The value at 2 K (18.3 μ_B) is unexpectedly high, based on previous studies with [3 × 3] Mn_9 and [4 × 4] Mn_{16} grids.[14,16,25] For the [3 × 3] grids, J values on the order of -5 cm^{-1} are observed, leading to a ground state of $S' = {}^5/_2$ and magnetic moments at 2 K of ~6 μ_B. In **22**, despite the odd number of metal ions, this is not the case, and there are clearly many spins still uncoupled at low temperature. M/H data at 2 K rise to a value of 56.5 Nβ at 5 T but show no sign of saturation. Modeling the exchange in such a large assembly of spins is clearly out of the question, but as expected, coupling within the grid is

antiferromagnetic. Further insights into the exchange picture will remain elusive until a more definitive structural picture can be obtained.

Conclusions

The organization of large numbers of paramagnetic metal ions in close proximity in polynuclear arrays can be achieved in a systematic way by choosing the ligand as the focal point if it can satisfy the coordination sphere requirements of the metal ion concerned. This "coordination algorithm" is expressed through the construction element of the ligand. [$n \times n$] square grids are relatively easy targets with six-coordinate metal ions because of the 90° arrangements of bonds, and this can be exploited with ligand pockets containing a *mer* grouping of donor atoms, leading to five-membered chelate rings, arranged in a linear fashion.

Polytopic hydrazone-based ligands are classic examples and result in the high yield formation of [2 × 2], [3 × 3], [4 × 4], and [5 × 5] square grids with a variety of paramagnetic metal ions. Both homometallic and heterometallic complexes have been produced. The close proximity of the μ-$O_{hydrazone}$-bridged metal ions leads to magnetic exchange coupling, with antiferromagnetic, ferromagnetic, and ferrimagnetic examples, some with high-spin ground states. The flat nature of the grids makes them suitable for surface applications, with the potential for single-molecule activity.

Acknowledgment. We thank the Natural Sciences and Engineering Research Council of Canada (NSERC) for financial support of this work.

Supporting Information Available: Crystallographic files (in CIF format) for **3**, **5**, **8**, **14**, **16**, **19**, and **21**. This material is available free of charge via the Internet at http://pubs.acs.org.

IC801078H